

Evaluating hypotheses for the initiation and development of *Alexandrium fundyense* blooms in the western Gulf of Maine using a coupled physical–biological model

Charles A. Stock², Dennis J. McGillicuddy Jr., Andrew R. Solow,
Donald M. Anderson

Woods Hole Oceanographic Institution, Woods Hole, MA 02543, USA

Accepted 27 June 2005

Available online 5 October 2005

Abstract

A coupled physical/biological model and observations are used to investigate the factors governing the initiation and development of an *Alexandrium fundyense* bloom in the western Gulf of Maine (WGOM) during the spring of 1993 (March 19–June 6). The physical circulation is simulated using a 3D primitive equation model forced by climatological sea-surface elevation and observed winds, irradiance, and river outflow. This is coupled with a biological model constructed from laboratory and field data that estimates the germination and growth rates of *A. fundyense* as a function of environmental conditions. Four biological model structures of increasing complexity are considered, with each structure representing a hypothesis for factors controlling bloom initiation and development. The model/data fit is optimized over the uncertainty in the parameters to which the model is most sensitive. The significance of changes in the model/data fit between model structures is quantified using a maximum likelihood ratio test.

The baseline biological model, which parameterizes growth as only a function of temperature, salinity, and light, severely over-estimates observed *A. fundyense* abundance in the late spring. It is thus rejected with greater than 99% confidence in favor of biological models that include a mortality term or a dependence of growth on dissolved inorganic nitrogen (DIN). The overall best-fit simulation uses both nitrogen dependence and mortality. However, simulations using one or the other of these factors could not be differentiated from the best-fit case with greater than 90% confidence. The best-fit model captures the general timing and magnitude of the observed bloom and some of its secondary features. However, considerable misfits may exist in the point-to-point comparison, and some regional misfits remain.

Diagnosis of the cell budget suggests that germination from a large cyst bed offshore of Casco Bay provides the majority of cells comprising spring *A. fundyense* populations within the WGOM. The size of the modeled bloom is largely set by the size of this cyst-driven source. Transport of cells from the eastern Gulf of Maine becomes increasingly important later in the spring. Net growth of the modeled *A. fundyense* populations is first limited by low water temperatures and then by the combined influence of nitrogen limitation and mortality. This results in low domain-averaged net growth rates ($<0.05 \text{ day}^{-1}$) throughout much of the simulation. However, rates are sometimes elevated locally and therefore add notable spatial structure to the bloom. Primary uncertainties within the biological model include spatial and temporal variability in mortality, and the influence of sediment dynamics and inter-annual variability in the cyst abundance on the

*Corresponding author. Tel.: +1 510 643 1252; fax: +1 510 643 1142.
E-mail address: cstock@whoi.edu (C.A. Stock).

size and spatial character of the cyst driven source. As the dynamics governing these processes become better understood, the approach herein can be extended to accommodate additional dynamical model complexity. However, the ability of the model/data comparison to constrain and support the inclusion of additional biological processes is dependent on both the availability of *A. fundyense* observations and the physical model skill.

© 2005 Elsevier Ltd. All rights reserved.

Keywords: Modeling; Statistical analysis; Algal blooms; Red tides; *Alexandrium fundyense*; Harmful algal blooms

1. Introduction

Blooms of the toxic dinoflagellate *Alexandrium fundyense* are annually recurrent phenomena in the Gulf of Maine during the spring and summer months. Toxins produced by *A. fundyense* lead to paralytic shellfish poisoning (PSP), a potentially fatal illness caused by consumption of shellfish from exposed regions. This public health risk necessitates rigorous monitoring of potentially affected areas and has led to repeated closures of shellfish beds along the coast and in the offshore waters of the Gulf of Maine (Shumway et al., 1988). Within the marine food web, PSP has been linked to mortality of larval and juvenile stages of fish (White et al., 1989), and even the death of marine mammals such as humpback whales (Geraci et al., 1989). An understanding of the factors that determine the distribution and abundance of *A. fundyense* within the Gulf of Maine is therefore of considerable scientific, economic, and public health interest.

In the spring, density contrasts between high-salinity slope water within the three deep basins of the Gulf of Maine and fresher coastal waters derived from the Scotian Shelf and local river input drive a mean counter-clockwise coastal surface current (Fig. 1, Brooks, 1985). This feature, referred to as the Maine Coastal Current (MCC), is characterized by a series of segments and branch points (Lynch et al., 1997). The direction of flow at the branch points is modulated by a diverse set of factors including wind, river input, bathymetric effects, and the strength of the geopotential low that generally forms over Jordan Basin in response to dense slope water in its interior (Brooks and Townsend, 1989; Brooks, 1994; Lynch et al., 1997; Pettigrew et al., 1998, 2005). *A. fundyense* blooms within the coastal region to the south and west of Penobscot Bay, herein referred to as the western Gulf of Maine (WGOM), are considered in this study. The region to the northeast is referred to as the eastern Gulf of Maine (EGOM). The segment of the coastal current within the WGOM is referred to

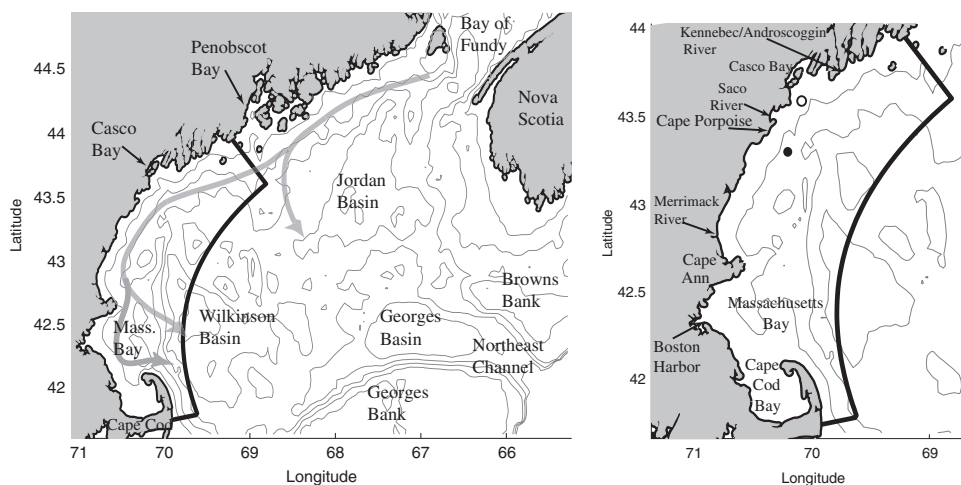


Fig. 1. Left panel: The Gulf of Maine and study region. The study domain is outlined by the thick black line. Depth contours are at 50, 100, 150 and 200 m. The direction of the flow of the Maine Coastal Current (adapted from Lynch et al., 1997) is shown as a thick gray line. Branch points off-shore of Penobscot Bay and Cape Ann are notable. Right panel: Close-up of the study region. River outflow locations are highlighted (the Charles River outflow is within Boston Harbor). The closed circle marks the location of the Cape Porpoise Mooring, while the open circle marks the location of the Portland Meteorological Buoy (NDBC station #44007).

as the WMCC, while the segment to the east is referred to as the EMCC.

Blooms of *A. fundyense* occurring in spring within the WGOM exhibit patterns in distribution and abundance largely consistent with the “plume advection hypothesis” (Franks and Anderson, 1992a; Anderson et al., 2005a). This hypothesis calls for the WMCC-driven transport of established populations of *A. fundyense* from the northeast to the southwest in close association with the buoyant plume of the Kennebec and Androscoggin rivers. Downwelling favorable winds accelerate the along-shore transport and trap the plume and associated cells against the coast. Upwelling favorable winds move the plume and cells offshore. An *A. fundyense* source is invoked in the Casco Bay region or further northeast. Patterns in shellfish toxicity show a mean progression from the Casco Bay area to the south that is consistent with this dynamic (Franks and Anderson, 1992b).

Extensive *A. fundyense* surveys undertaken in the WGOM during the spring of 1993 (Anderson et al., 2005a) provide an additional means of testing the plume advection hypothesis and to further explore the underlying dynamics. However, strong advective and mixing processes in the WGOM can produce a geographic separation between observed *A. fundyense* populations and their source regions. This makes the underlying bloom dynamics difficult to understand from survey data alone. In this study, a coupled physical/biological model is used to investigate the influence of biological processes and physical transport on the observed *A. fundyense* distribution. The physical component of the model provides an estimate of the currents and hydrography, while the biological component provides an estimate of the germination and net growth rates of *A. fundyense* as a function of environmental conditions.

Considerable uncertainty exists within the biology, and five potential biological model structures are considered (Table 1). The first four structures are nested: the more complex model structures reduce to the more simple cases when specific parameter values are set to zero. The first structure is the baseline case, which poses net growth as only a function of temperature, light, and salinity. The next two structures build upon the baseline model by adding the possibility of mortality and nutrient dependence, respectively. The fourth considers nutrients and mortality in combination. The fifth case imposes the condition that growth and

Table 1

Summary of the growth rate dependence for the 5 biological model structures

Structure	Growth rate dependence	Mortality
Baseline	<i>T, S, E</i>	No
Mortality	<i>T, S, E</i>	Yes
Nutrients	<i>T, S, E, N</i>	No
Mortality and nutrients	<i>T, S, E, N</i>	Yes
Zero net growth	NA	NA

T = temperature, *S* = salinity, *E* = irradiance, *N* = nutrients (i.e. dissolved inorganic nitrogen), NA = not applicable (see text).

mortality are in balance, resulting in zero net growth throughout the domain at all times. This very precise structure does not strictly fit into the nested set described above (this is clarified and discussed in Section 2). It is used as a limiting case to understand the impact of net-growth on the magnitude and spatial/temporal characteristics of the *A. fundyense* bloom.

Each of these biological model structures constitutes a different hypothesis for the factors controlling the initiation and development of *A. fundyense* blooms in the WGOM. Hypotheses are evaluated through a quantitative, statistical comparison of model results with 1993 survey data. The goal is to identify a set of dynamics capable of recreating the general timing and magnitude of bloom events, not the detailed structure of the bloom. The steps are summarized as follows:

1. The model/data fit is optimized for each hypothesized biological model structure over the uncertainty in the parameters to which the model is most sensitive.
2. A maximum likelihood ratio test (MLRT) is used to evaluate the significance of changes in the optimal model/data fit.
3. A simpler model structure is rejected in favor of one that is more complex if the improvement gained by adding an additional factor or factors is statistically significant.
4. Simulations are assessed and diagnosed to gain insight into bloom dynamics.

Model diagnosis focuses on identifying the primary source of *A. fundyense* cells contributing to spring toxicity in the WGOM and on elucidating the factors controlling bloom development. It is stressed that the methodology outlined above and

described in detail below is iterative in nature. The model/data misfits encountered under the most basic hypothesis considered herein suggest possible alternatives that may better explain the observations. In a like manner, the model/data misfits remaining at the conclusion of this analysis will be discussed, as they suggest avenues for further model improvement.

2. Methods

2.1. The field data

A field program including five ship surveys and mooring deployments carried out in 1993 provides the observational basis for this study (Geyer et al., 2004; Anderson et al., 2005a). The duration of each survey was 2–3 days, and they were spaced

approximately two weeks apart (April 12–14, April 28–30, May 10–13, May 24–27, June 4–6). *A. fundyense* cell counts were taken at the surface (Fig. 2, top panel) and, for ~75% of the stations, at 10 m. Hydrographic and nutrient data, including phosphate, silicate, nitrate, nitrite, and ammonium (Martorano and Loder, 1997), were also collected. Nutrient ratios consistently suggest dissolved inorganic nitrogen (DIN) (Fig. 2, bottom panel) to be limiting relative to phosphorous assuming Redfield stoichiometry. Currents were measured at a mooring near Cape Porpoise (Fig. 1) using a vector-measuring current meter (VMCM) at 5 m, and vector-averaging current meters (VACM) at 27 and 50 m. The near-surface measurements required a 25° clockwise rotation to correct for compass error believed to be due to interference with battery packs in adjacent sensors (see Geyer et al., 2004 for

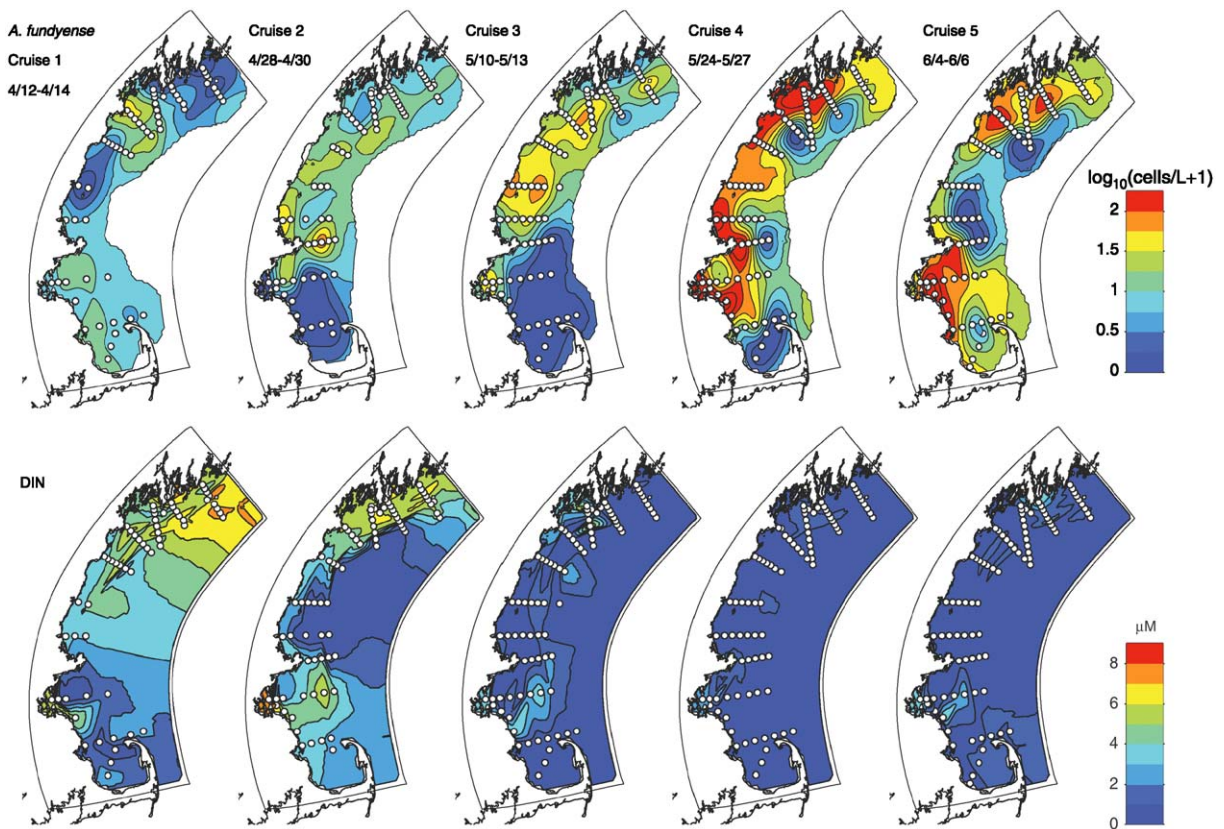


Fig. 2. The RMRP surface *A. fundyense* and dissolved inorganic nitrogen (DIN) field data. White circles are observation points. Columns correspond to cruises 1–5. Top panel: The observed surface distribution of *A. fundyense* during the spring 1993 RMRP surveys (Anderson et al., 2005a). The contour interval is 0.25. Note that color scale was chosen to capture the variation in the majority of the data. Contours continue at the specified interval above the maximum colorbar value in isolated areas of high concentration (e.g., the region near Boston Harbor during cruise 4). Bottom panel: Surface dissolved inorganic nitrogen (DIN, μM) measured during the 1993 RMRP surveys (Martorano and Loder, 1997). The contour interval is 1.0 μM .

Table 2
Physical model forcing

Forcing	Source/description
Sea surface elevation	M_2 tide from Gulf of Maine tidal model (Lynch and Naimie, 1993) Mean elevation from bi-monthly climatology (Naimie et al., 1994)
Wind	Portland off-shore buoy (NDBC #44007), applied throughout domain and translated to shear via Large and Pond (1981)
River discharge	USGS stream gauges at 4 major rivers: Charles, Saco, Merrimack, and the Kennebec/Androscoggin
Boundary T, S	Interpolated and extrapolated from mooring and survey data
Initial T, S	spatially averaged climatology (Naimie et al., 1994)
Heat flux	Shortwave radiative heat flux from land-based sensor at Woods Hole Sensible and latent heat fluxes estimated using Portland off-shore buoy data and the bulk formulae of Large and Pond (1982) Longwave flux estimated using Portland off-shore buoy data and relationships of Berliand and Berliand as described in Fung et al. (1984)

details). The correction has a minor influence on the along-shore flow, but the surface cross-shore component should be treated with caution.

2.2. The physical model

The circulation is modeled using the Estuarine, Coastal and Ocean Model (ECOM) (Blumberg and Mellor, 1987). This model solves the primitive equations using finite differences on a curvilinear orthogonal grid. ECOM has been used extensively to model coastal and estuarine flows (Blumberg et al., 1993) and has previously been applied in the Gulf of Maine region (Signell et al., 1993; McGillicuddy et al., 2003). The model configuration is essentially that used in McGillicuddy et al. (2003). The study domain (Fig. 1) is covered by a grid of 130 cells in the alongshore direction and 70 in the cross-shore. Grid cells range in size from 1.5 to 3 km. Twelve sigma layers (i.e. each layer is a constant fraction of the water depth) are specified in the vertical with increased resolution near the surface in order to better resolve river plume dynamics. Vertical mixing is calculated with the Mellor-Yamada level 2.5 turbulence closure (Mellor and Yamada, 1982; Galperin et al., 1988), and horizontal mixing is calculated using the method of Smagorinsky (1963).

Forcing (Table 2, Fig. 3) was chosen to capture the principal aspects of the large-scale circulation and hydrography in the WGOM, particularly the transport associated with the WMCC and the vernal warming of surface waters. The duration of the simulation is from March 19 to June 6. In addition to heat flux calculations described in Table 2,

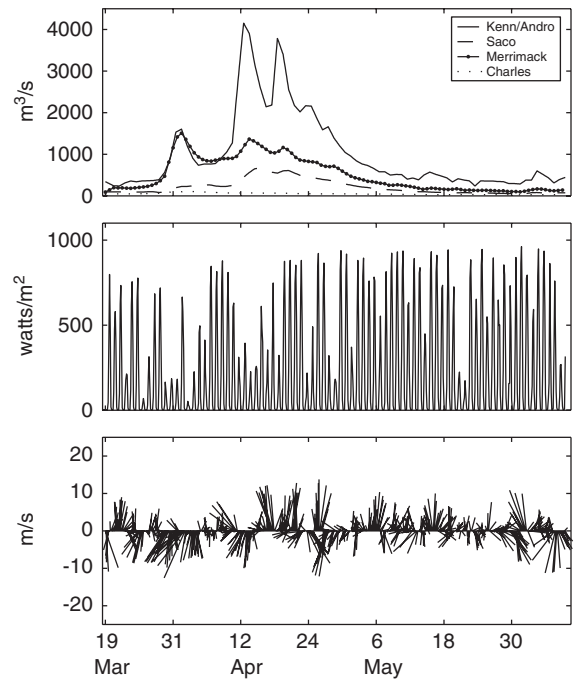


Fig. 3. The physical model forcing. Top panel: River outflow in $\text{m}^3 \text{s}^{-1}$ for each of the four modeled river inputs within the domain. Middle panel: Short wave radiation flux (W m^{-2}). Bottom panel: Wind speed and direction (m s^{-1}).

surface-temperature fidelity is ensured by relaxing toward the observed sea-surface temperature using a nudging term proportional to the difference between modeled (T) and observed (T_{obs}) surface temperatures (Ezer and Mellor, 1992; He and Weisberg, 2002):

$$Q = Q_{\text{calc}} + \rho_w c_p C(T - T_{\text{obs}}), \quad (1)$$

Table 3
Parameters in the biological model

Symbol	Definition	Units	Range	Sources
K_N	Half-saturation constant for nutrient limited growth	μM	0–3	Eppley et al. (1969), Eppley and Thomas (1969), Lomas and Glibert (2000), Carpenter and Guillard (1971), MacIsaac et al. (1979), and Sommer (1991)
m	Spatially and temporally averaged mortality	day^{-1}	0–0.3	See text
$\mu_{\max}(T_{\text{opt}}, S_{\text{opt}})$	The maximum growth rate under optimal temperature and salinity conditions	day^{-1}	0.46–0.70	Cullen (unpublished data), Langdon (1987), Etheridge and Roesler (2005), Watras et al. (1982), Keafer and Kulis (unpublished data) ^a
μ_0^r	The maintenance respiration rate	day^{-1}	0.15–0.25	Cullen (unpublished data)
α_g	The growth efficiency	$\text{day}^{-1} \text{W}^{-1} \text{m}^2$	0.017–0.056	Cullen (unpublished data)
d_g	The mean depth of sediment over which cysts are able to germinate and contribute to the bloom	cm	0.5–1.5	Anderson et al. (2005b)
E_{igt}	Light level for germination under “light” conditions	W m^{-2}	1.2–3.6	Anderson et al. (2005b)
E_{drk}	Light level for germination under dark conditions	W m^{-2}	0.1% of I_{igt} to 10% of I_{igt} .	Anderson et al. (2005b)
k_w	Mean diffuse attenuation in water column	m^{-1}	0.15–0.25	Townsend et al. (2001)
k_s	Mean diffuse attenuation in the sediment	mm^{-1}	2–5	Kuhl and Jorgensen (1994)
w_a	Vertical swimming speed	m day^{-1}	5–15	Bauerfeind et al. (1986), and Kamykowski et al. (1992)

^aSources used for formulation of the growth versus temperature dependence polynomial are: Etheridge and Roesler (2005), Langdon (1987), Watras et al. (1982), and Keafer and Kulis (unpublished data). Sources used for the salinity dependence polynomial are: Etheridge and Roesler (2005) and Prakash (1967).

where Q_{calc} is the heat flux (W/m^2) calculated by the bulk formulae, ρ_w the water density, c_p the specific heat of seawater at constant pressure, and C a constant, which is given a value of 2 m/day. The observed surface temperatures are provided by 11 maps covering the simulation period constructed from 8 day best AVHRR Oceans Pathfinder SST (PO.DAAC, 1985) satellite data using the objective analysis algorithm of Bretherton et al. (1976) as implemented by Hendry and He (1996).

2.3. The biological model

Alexandrium species are characterized by a complex life cycle that includes both a resting cyst and a vegetative cell (Anderson, 1998). The transition between resting and vegetative stages occurs through the process of germination. The biological model used in this study and described in detail below is a single-component model containing

parameterizations of *A. fundyense*¹ germination, as well as subsequent growth and swimming behavior (summarized in Table 3 and Fig. 4). Ecosystem effects on *A. fundyense* abundance are parameterized through approximations of their influence on the rates within the *A. fundyense* population dynamics model. The biological model is necessarily simplified, and it is not expected that all scales of variability within the *A. fundyense* bloom will be reproduced. This is consistent with the goals of the

¹It is recognized that two forms of *Alexandrium* can be responsible for shellfish toxicity in the WGOM: *A. tamarense* and *A. fundyense*. We consider these to be varieties of the same species (Anderson et al., 1994; Scholin et al., 1995). Neither antibody nor oligonucleotide probes can distinguish between them, only detailed analysis of the thecal plates on individual cells can provide this resolution. *A. fundyense* is therefore used to refer to both forms.

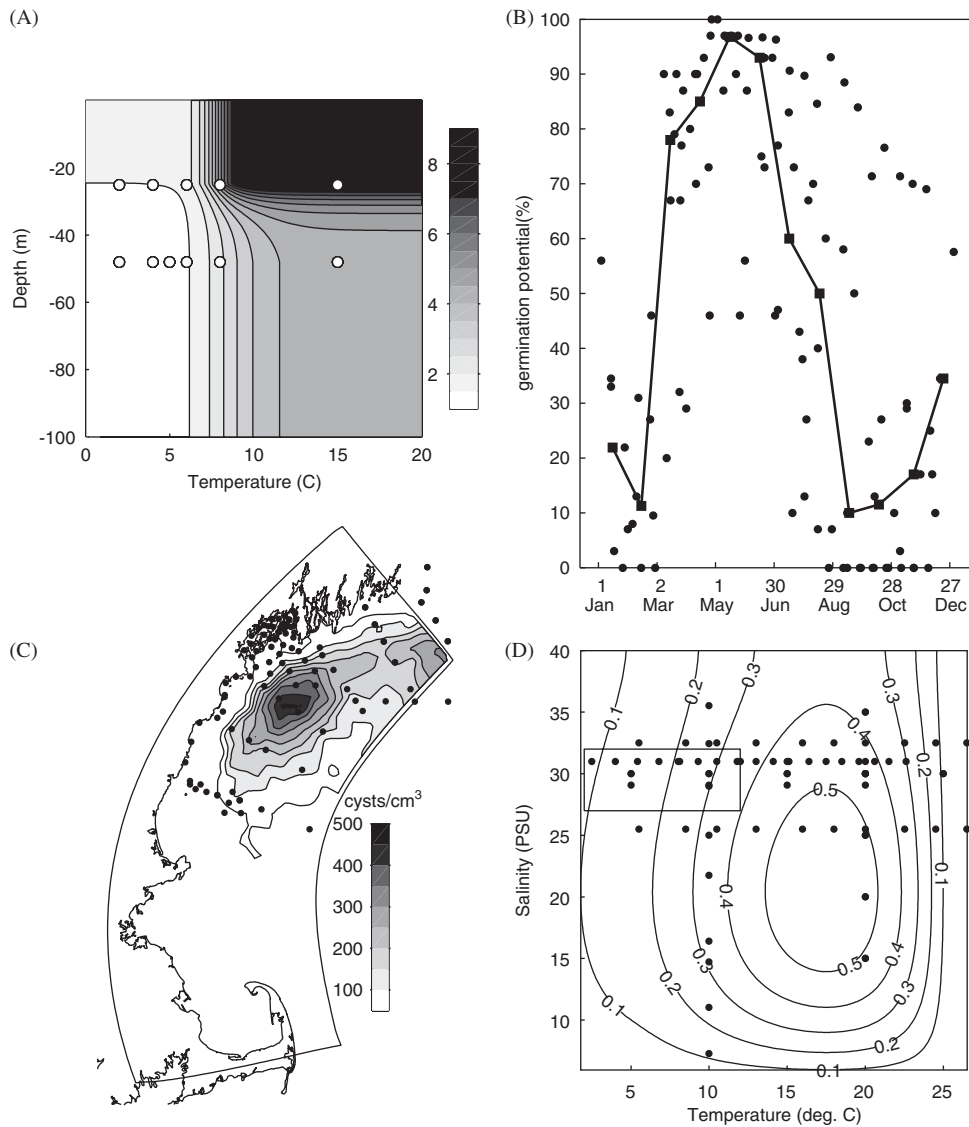


Fig. 4. (A–D) The biological model summary. All plots show observations as dots. (A) The germination rate (%/day) at the sediment surface as a function of temperature and light. Light has been converted to depth using a diffuse attenuation coefficient (k_w) of 0.2 m^{-1} and a representative day-averaged surface irradiance of 350 W m^{-2} . (B) The endogenous clock function. The connected squares give the estimated germination potential for each month based on a median filter of data from seven different cyst isolates within the Gulf of Maine. This curve is normalized to produce a factor between 0 and 1 that scales the germination rate. (C) The cyst map (cysts cm^{-3}) in the top cm. (D) The growth rate (day^{-1}) as a function of temperature and salinity. This plot uses $\mu_{\max}(T_{\text{opt}}, S_{\text{opt}}) = 0.58 \text{ day}^{-1}$. The boxed area contains the range of T , S conditions encountered over the vast majority of the domain for the duration of the simulations.

analysis (i.e. recreating the timing and magnitude of the bloom events). Neglected complexity should be considered intrinsic to the hypotheses: neglect is equivalent to the assumption that the importance of a given process is of second-order relative to those included at the space and time scales of interest. Model data misfits may then be analyzed in light of this neglected complexity and new hypotheses formulated.

2.3.1. Germination

Rates of *A. fundyense* cyst germination are regulated by an endogenous circannual clock (Anderson and Keafer, 1987; Matrai et al., 2005) and by a suite of environmental factors including temperature (Anderson, 1980), light, and oxygen, the absence of the latter preventing germination entirely (Anderson et al., 1987). The construction of a germination function based on laboratory and

field data is described in detail in Anderson et al. (2005b). Briefly, laboratory data were used to estimate cyst germination rates (G) as a function of bottom-water temperature (T) and non-spectral irradiance (E) (Fig. 4A). The influence of the endogenous clock was accounted for by multiplying the germination rate by an endogenous clock factor (EC, Fig. 4B), which is the ratio of the germination potential at any time (t) relative to the maximum potential:

$$G(T, E, t) = EC(t) \times G(T, E). \quad (2)$$

The irradiance experienced by the cysts is the end result of exponential attenuation within the water column and within the sediment (decay coefficients k_w and k_s , respectively). The rate is then averaged over the estimated depth of sediment (d_g) assumed oxygenated and over which newly germinated cells can reach the water column during the bloom season. This “germination depth” was estimated using the penetration of short-lived isotopes, cyst fluorescence measurements, and biochemical measurements within the sediment (see Anderson et al., 2005b), and a range from 0.5 to 1.5 cm is considered.

The resulting germination function is applied to a map of the cyst concentration within the top 1 cm of sediment from surveys taken between 1997 and 2003 (Fig. 4C). The vast majority of the cyst measurements were taken in 1997, and it is assumed that the primary features of the cyst map are robust over the four years separating the cyst and RMRP surveys (see supporting discussion in Anderson et al. (2005b) and McGillicuddy et al. (2005)). The resulting flux of cells from germination (F_g) is

$$F_g = \int_0^{d_g} G(T, E(z), t) \times [\text{Cysts}/\text{cm}^3]_0 dz, \quad (3)$$

where $[\text{Cysts}/\text{cm}^3]_0$ is the initial concentration of cysts in the top centimeter. Eq. (3) yields units of cells/(cm² day), which are translated to cells/(m² s) for entry into the model (see Section 2.4). The flux is calculated relative to the initial number cysts to be consistent with the laboratory experiments upon which they are based. It is notable that the validity of the above expression requires the assumption that the cyst concentration is uniform over the top 1.5 cm. This is justified based on the high correlation (0.85) and the similar mean concentrations (87 cysts/cm³, 106 cysts/cm³) of cysts from 0–1 to 1–3 cm sediment layers within the study domain.

2.3.2. Swimming

Newly germinated cells swim upward at w_a m/day (Table 3) until the mean depth of the 1% light level ($z_1 = 21$ m) is reached. It is assumed that there is no cell mortality during this transit. Above this level, diminution of the vertical swimming speed to the natural boundary condition of $w_a = 0$ at $z = 0$ is specified in order to match the observed vertical distribution of *A. fundyense*. The ratio of the mean abundance at the surface to that at 10 m for stations with abundance measurements at both depths is 2:1 and there is a strong correlation between the measured abundances at the two depths for the same station (correlation coefficient of 0.71 after log-transformation). It was found that attenuating the swimming speed with

$$w_a(z < z_1) = w_a(z > z_1) \times \left(1 - \tanh\left(\frac{(z_1 - z)}{10}\right) \right) \quad (4)$$

produced ratios of mean surface to mean 10 m abundance between 1.75:1 and 2.25:1 for a broad range of biological model parameter values. More complex migration strategies have been observed for *A. fundyense* (Anderson and Stolzenbach, 1985; MacIntyre et al., 1997). However, in the WGOM, *A. fundyense* have not been observed to engage in strong coordinated migrations either in the laboratory or the field (Poulton, 2001), so such behavior is omitted here.

2.3.3. Growth

The *A. fundyense* growth function is dependent on temperature (T), salinity (S), non-spectral irradiance (E) and, for model structures containing nutrient dependence, the DIN concentration. The temperature dependence was formed by fitting a cubic polynomial to *A. fundyense* growth data collected for different isolates in the region ($R^2 = 0.79$, see Table 3 for references). This function was then normalized to form a factor between 0 and 1 that expresses the degree of temperature limitation relative to the maximum growth observed:

$$\begin{aligned} f(T) &= -0.000513 T^3 + 0.0160 T^2 \\ &\quad - 0.0867 T + 0.382 \quad T \geq 5^\circ\text{C}, \\ f(T) &= f(T = 5) - 0.0343(5 - T) \quad T < 5^\circ\text{C}. \end{aligned} \quad (5a, b)$$

The linear extrapolation below 5 °C was used to prevent irregular extrapolation in regions not well constrained by data. The salinity dependence was

formed in a similar way ($R^2 = 0.45$)

$$g(S) = 0.0000882S^3 - 0.00808S^2 + 0.220S - 0.872. \quad (6)$$

These two factors scale the light and nutrient saturated growth rate at optimal temperature and salinity, $\mu_{\max}(T_{\text{opt}}, S_{\text{opt}})$, to determine the light saturated growth rate at any T, S (Fig. 4D)

$$\mu_{\max}(T, S) = \mu_{\max}(T_{\text{opt}}, S_{\text{opt}}) \times f(T) \times g(S). \quad (7)$$

The light dependence takes the form suggested by Platt and Jassby (1976) for photosynthesis-irradiance relationships and used by Langdon (1987, 1988) in studies of phytoplankton growth (see Table 3 for definitions and units):

$$\begin{aligned} \mu(E, T, S) \\ = (\mu_{\max}(T, S) + \mu_0^i) \tanh\left(\frac{\alpha_g E}{(\mu_{\max}(T, S) + \mu_0^i)}\right) - \mu_0^i. \end{aligned} \quad (8)$$

Nutrient dependence is modeled by the Monod formulation with half-saturation K_N :

$$\mu(\text{DIN}, T, S) = \mu(T, S) \times \frac{[\text{DIN}]}{K_N + [\text{DIN}]}. \quad (9)$$

This dependence of the growth rate on nutrients (i.e. DIN concentration in this application) can be problematic in unsteady conditions due to potential variability in nitrogen uptake physiology and the internal nitrogen cell quota (e.g., Conway and Harrison, 1977; Droop, 1983). Such variability has been observed in *Alexandrium* species (Flynn et al., 1996). However, while the Monod formulation is limited in its ability to represent detailed nitrogen metabolism, it is valid for assessing the average level of the dependence of growth on ambient DIN and should be interpreted in this way. The range of K_N considered herein was chosen to encompass the range of half-saturation constants for nitrogen dependent growth and uptake commonly encountered in the phytoplankton literature (Table 3). The limiting case of $K_N = 0 \mu\text{M}$ asserts that *A. fundyense* is not significantly DIN limited during the simulation period.

The evolution of the DIN field is specified based on survey data (i.e. Fig. 2B). The lack of a dynamic link between the modeled *A. fundyense* concentration and DIN is justified on the basis that typical peak *A. fundyense* cell concentrations in the WGOM ($\sim 10^2$ – 10^3 cells/L) are small relative to the total abundance of other phytoplankton species

($\sim 10^4$ – 10^6 cells/L without inclusion of nano- or picoplankton abundance (Marshall, 1984)). *A. fundyense* therefore contributes little to the large scale nutrient evolution. A linear interpolation is used to specify nutrients at times between cruises. The most limiting factor of light or nutrients determines the ultimate growth rate as per Liebig's law of the minimum (Liebig, 1845):

$$\mu(E, \text{DIN}, T, S) = \min(\mu(E, T, S), \mu(\text{DIN}, T, S)). \quad (10)$$

2.3.4. Mortality

Mortality (m) is defined loosely here as a vegetative cell removed from the water column. It is meant to represent the losses of *A. fundyense* by cell mortality, zooplankton grazing, and encystment. Grazing losses inflicted on *A. fundyense* are a complex function of both the heterotrophic and autotrophic communities (Teegarden and Cembella, 1996; Turner and Tester, 1997). Encystment is generally thought to occur in response to adverse environmental conditions and has been triggered by nutrient limitation in the laboratory (Anderson et al., 1984; Anderson and Lindquist, 1985). However, the precise thresholds and rates for nutrient-driven encystment have been difficult to characterize, and it has been equally difficult to observe in the field (Anderson, 1998). Mortality is therefore applied as a constant average rate (day^{-1}). The intent of applying mortality in such a rudimentary way is to evaluate the necessity of a first-order loss term to recreate the observed bloom magnitude, given knowledge of the source and growth characteristics. The range in Table 3 is chosen to allow the possibility of negligible mortality rates to rates that would overcome all but very swift growth. The hypotheses containing this term assume that space/time variability in mortality during bloom initiation and development is of secondary importance to this overall mean rate.

2.4. The coupled model

The final equation governing the evolution of *A. fundyense* within the domain is:

$$\frac{\partial C}{\partial t} + \nabla \cdot ((v + w_a)C) = \nabla \cdot K \nabla C + \mu C - mC + F_g, \quad (11)$$

where C is the concentration of *A. fundyense*, v the fluid velocity, K the diffusivity, and F_g is entered as a source into the bottom grid cells. The initial

concentration of *A. fundyense* is set to 0 everywhere, as the beginning of the run (March 19) is generally before the start of the bloom season. Observed cell concentrations along the northern-most transect are extrapolated onto the northern boundary to provide the EGOM inflow boundary condition. Concentrations along the other boundaries are assumed 0. Interior concentrations are advected out during outflow at the boundaries, and boundary concentrations are relaxed linearly back to the specified values during subsequent inflows. Time scales for this relaxation were chosen to represent the relative strength and duration of inflow and outflow events (0.5 days along the northern boundary, 2 days along the eastern boundary, and 4 days to the South). The model solution is not overly sensitive to this choice, as relaxation times along the northern boundary ranging from 0 to 2 days only cause ~10% variability in the influx of cells.

2.5. Model/data comparison

2.5.1. The statistical description of the model/data misfit

The method of maximum likelihood is used to determine the biological model parameter values that optimize each dynamical model structure's ability to match observations and to evaluate the performance of each structure relative to the others. Within this methodology, model/data misfits are viewed stochastically and the optimal simulation is defined as the combination of parameter values that maximizes the joint probability of the misfits. This requires the definition of a "misfit model", consisting of several assumptions regarding the stochastic properties of the misfit. The misfit model rarely can be determined on purely theoretical grounds, but is of considerable importance as it implicitly determines the misfit weights. The description of the misfit provided in this section is thus best thought of as a proposed misfit model that must be verified before ratification of any results. This verification will be addressed in Section 3.3.

The fact that *A. fundyense* concentrations vary over several orders of magnitude suggests that differences between the model and data may be normally distributed after log-transformation. The misfit is thus defined as:

$$\varepsilon_i = \ln(c_{\text{obs},i} + 1) - \ln(c_{\text{mod},i} + 1), \quad (12)$$

where $c_{\text{obs},i}$ is the observed *A. fundyense* concentration at point i , and $c_{\text{mod},i}$ the model output (in cells/

L) at i . One is added to all values so that zero cell concentrations can be included in the analysis. The likelihood is then defined as:

$$L(\theta_1 \dots \theta_n; \varepsilon) = \frac{\exp\left(-\frac{1}{2} \times \varepsilon^T C_{\varepsilon\varepsilon}^{-1} \varepsilon\right)}{(2\pi)^{M/2} \sqrt{\det(C_{\varepsilon\varepsilon})}} \quad (13)$$

which is simply the joint probability for a normally distributed set of model/data misfits (e.g., Wunsch, 1996). In this case, ε is a vector of $M = 386$ misfits, T is the transpose, "det" is the determinant, and $C_{\varepsilon\varepsilon}$ is the spatial/temporal covariance matrix. The central diagonal of the covariance matrix contains the misfit variance (σ^2). Spatial covariance between any two misfits i, j is represented with exponential decay terms in the along-shore (r_x) and cross-shore (r_y) directions:

$$C_{ij} = \rho_{\Delta t} \sigma^2 \exp\left(-r_y \sqrt{\Delta y^2 + \left(\frac{r_x}{r_y} \Delta x\right)^2}\right). \quad (14)$$

This simple elliptical form (note that the exponent can be rewritten as: $-\sqrt{r_y^2 \Delta y^2 + r_x^2 \Delta x^2}$) was chosen because the along-shore spatial decorrelation scale of the observed patches (e-folding ~20–25 km) is slightly larger than the cross-shore (e-folding ~15 km). Temporal correlation is introduced with the factor $\rho_{\Delta t}$. The roughly equal bi-weekly spacing of the cruises makes it possible to use the number of cruises separating any two observations as a proxy for temporal lag. Thus, $\rho_{\Delta t=1}$ corresponds to the correlation between points at the same spatial location, but separated by one cruise. For points taken during the same cruise, this factor ($\rho_{\Delta t=0}$) has a value of 1. Only correlations between points separated by one or two cruises are considered herein.

The parameters describing the covariance matrix (σ^2 , r_x , r_y , $\rho_{\Delta t=1}$, and $\rho_{\Delta t=2}$) are chosen to maximize L for the set of misfits produced by each choice of the biological model parameters. A simplex parameter space search (Press et al., 1985) is enlisted for this purpose. Multiple starting points were used to test for the presence of multiple minima, and no such occurrences were found. The likelihood for normally distributed misfits (13) generally increases as the misfit variance and spatial/temporal scales decrease, revealing a close relationship with commonly used least-squares parameter estimation. Indeed, the parameter estimates yielded by the two methods correspond precisely when misfits are normally distributed and independent. Generalized

least squares can extend this correspondence to misfits that covary in space or time. It is notable that the misfit model parameters provide estimates of the spatial and temporal scales of the misfit. These estimates and their relationship to the deterministically resolved scales of motion in the physical model provides useful information when considering further biological model improvement relative to limitations of the physical simulation and observations (see Sections 3.4 and 4.3).

2.5.2. Optimization over the biological model parameters

To compare the performance of the different model structures in Table 1, the likelihood (L) of the misfits must be maximized over the uncertainty in the biological model parameters included within each structure (Table 3). The search for optimal parameter values was carried out manually with a large set of numerical simulations. Due to the large number of parameters, it is not practical to systematically evaluate the entire range of parameter space. The optimization process was therefore restricted to parameters to which the model was most sensitive. These parameters were identified using the bulk sensitivity metric:

$$SM(t) = \frac{\left(\iiint_{\text{domain}} C(x, y, z, t) dx dy dz \right)_{\theta=\theta_{\text{high}}}}{\left(\iiint_{\text{domain}} C(x, y, z, t) dx dy dz \right)_{\theta=\theta_{\text{low}}}}, \quad (15)$$

where C is the concentration of *A. fundyense*. Multiplied by 100, this factor is the percent change in the total number of cells in the domain induced by varying each parameter θ (Table 3) from the value producing the lowest *A. fundyense* abundance (θ_{low}) to the value producing the highest (θ_{high}). Uncertainty in two parameters, μ_{max} and d_g , generally controls greater than 90% of the variability in this metric for the baseline model (Fig. 5). The likelihood was thus maximized only over the uncertainty in μ_{max} and d_g for the baseline model, m was added for the mortality only case, K_N for nutrients only, and K_N and m for mortality and nutrients. For model structure 5, optimization was carried out over d_g only, as growth and mortality are assumed in balance. The search space in all cases is limited to the ranges in Table 3, and the remaining biological model parameters are given central values within their uncertainty range.

2.5.3. Testing hypotheses: The maximum likelihood ratio test

The MLRT is used to estimate the significance of differences in the optimal fit for the different model structures. The test compares the likelihood of a null hypothesis (L_0) to the likelihood of an alternative (L_1) that allows one or more of the biological model parameters set by the null hypothesis to vary over their uncertainty. For example, in comparing model structures with and without mortality, the following ratio is formed:

$$\lambda = \frac{L(\mu_{\text{max}}, d_g, m = 0; \varepsilon)}{L(\mu_{\text{max}}, d_g, m; \varepsilon)} = \frac{L_0}{L_1}. \quad (16)$$

Note that the parameter space in the denominator of the ratio has an additional degree of freedom—the alternative hypothesis is the more complex model structure. As such, the maximum likelihood in the denominator will be at least as large as that of the numerator. As this ratio becomes much less than 1, the null hypothesis becomes less likely than the alternative, and rejection of the null hypothesis is supported.

The degree of significance with which the null hypothesis can be rejected is estimated by invoking the properties of the MLRT for large sample sizes. It can be shown (Cox and Hinkley, 1974) that, if the null hypothesis is true the quantity:

$$-2 \ln(\lambda) = -2(\ln(L_0) - \ln(L_1)) \quad (17)$$

will asymptotically approach a χ^2 distribution with degrees of freedom equal to the additional number of free parameters in the alternative hypothesis. The ability to reject a null hypothesis can thus be estimated based on the size of $-2 \ln(\lambda)$ relative to what is expected from a χ^2 statistic with the appropriate number of degrees of freedom.

It is impossible to define precisely a change in the number of degrees of freedom between the fifth model structure and the others. As previously noted, this structure represents a very exact hypothesis: it calls for patterns in mortality and growth that cancel to give zero net growth at all times and in all places. It is impossible to attain such a condition within the parameter ranges of Table 3. If parameter values were not restricted to these ranges, zero net growth could be accomplished by setting μ_{max} and m to 0 day^{-1} . However, such a model would be rejected within the present methodology because it requires an unrealistic value of μ_{max} (such considerations could be formalized in future efforts by implementing Bayesian statistical

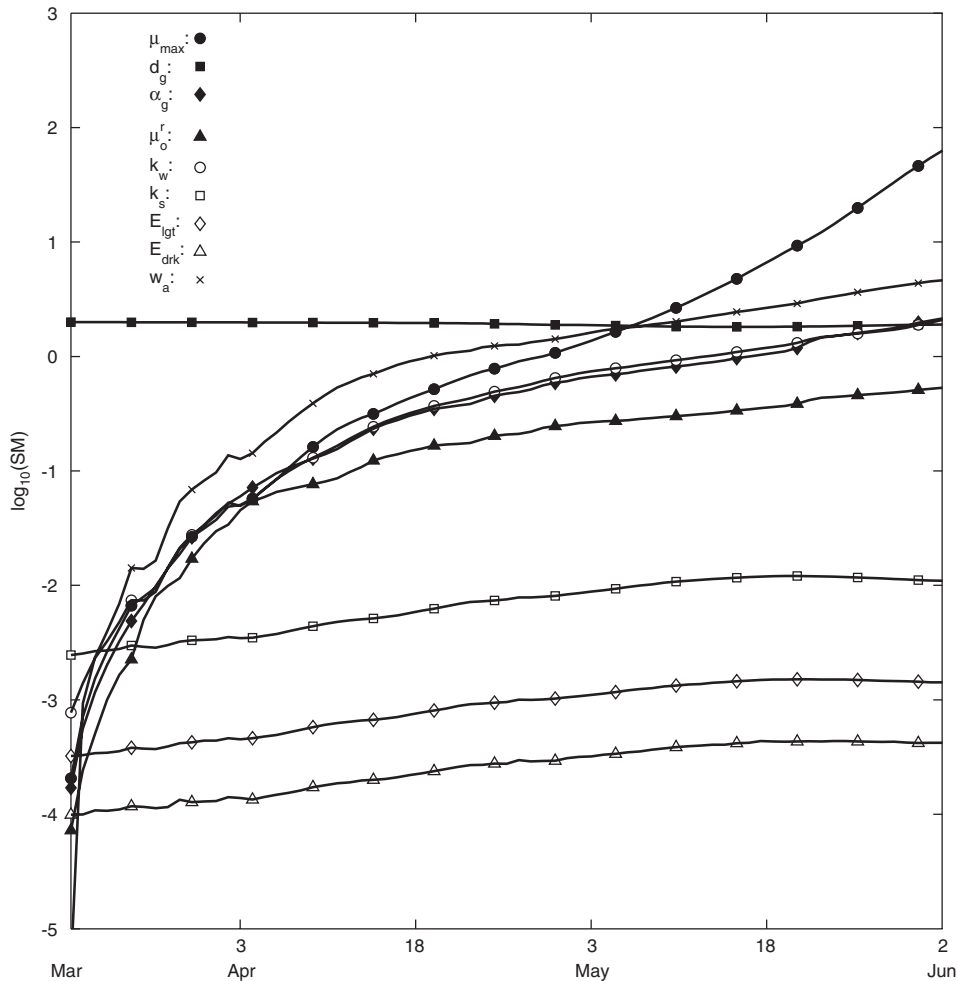


Fig. 5. The baseline model sensitivity. The germination depth (d_g) dominates the baseline model sensitivity until early May, when it is eclipsed by the maximum growth rate (μ_{\max}).

techniques). Furthermore, the hypothesis that μ_{\max} and $m = 0 \text{ day}^{-1}$ is not equivalent to the condition imposed by the fifth model structure: that $\mu = m$ for all space and time. The former statement only represents one possible means of achieving the latter condition. Fortunately, such issues with the analysis of this last structure do not undermine its purpose as an illustrative comparison simulation useful for assessing the impact of net growth on the modeled bloom.

3. Results

3.1. The physical circulation

Comparison of the modeled and observed currents at the Cape Porpoise mooring shows that the model matches the primary characteristics of the

WMCC in the spring of 1993 (Fig. 6). One discrepancy is that the modeled currents are on average 2.5–3 cm/s faster than those observed. Much of this difference is accrued during the period between April 7 and 23. The precise origin of this discrepancy and its persistence over the model domain is uncertain, but its potential influence on the biological misfit will be revisited during the discussion. Directionally, the average modeled and observed currents are within 20° at all depths. Both the modeled and observed surface currents exhibit a similar response to the wind, veering further east (off-shore) during periods of upwelling (e.g., mid to late April). The mean surface circulation (Fig. 7) is consistent with the climatology of Lynch et al. (1997). The primary difference between the climatology and the model is the decreased flow magnitude in March/April for the 1993 simulation.

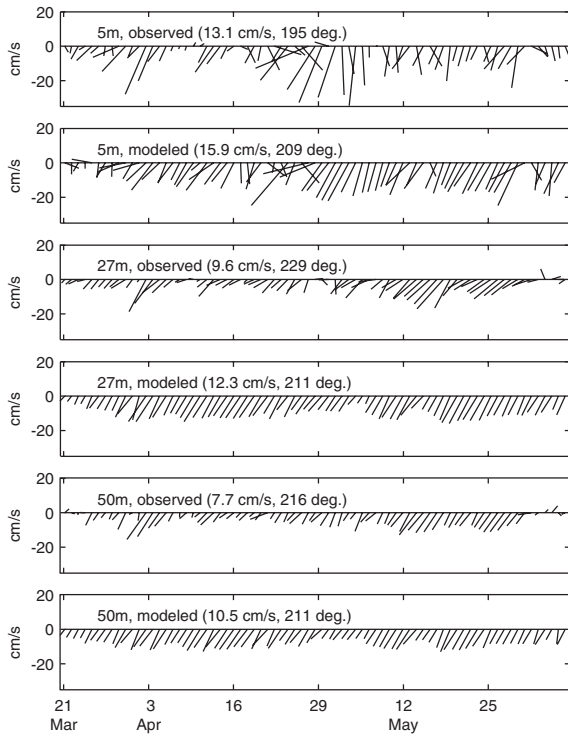


Fig. 6. Comparison of modeled and observed current speed and direction at the Cape Porpoise mooring. The average magnitude and direction of the current is given in parentheses. Direction is given in degrees on the compass rose. The approximate along-shore direction at the Cape Porpoise mooring is 210° . Note that there is some uncertainty in the direction of the observed current at 5 m (as outlined in Section 2.1).

This is supported by the mooring comparison, and is therefore attributed to the non-climatological elements of the physical simulations (Table 2).

The vernal warming of sea-surface temperatures is well captured by the model (Fig. 8, top panel), although there is a slight tendency for the modeled warming to lag behind the observations. The majority of this signal was captured by the observed and modeled heat flux, with the nudging term adding an average of 18% to the incident short-wave irradiance averaged over the day. Part of this latter term is likely compensation for an over-estimation of the heat transfer below 10 m in the model, which results in a somewhat broader thermocline than observed (not shown). This is attributable to either overly vigorous vertical mixing of heat or an underestimate of the attenuation of shortwave radiation between 0 and 10 m.

The modeled and observed surface salinity both show a strong response to the wind (Fig. 8, bottom

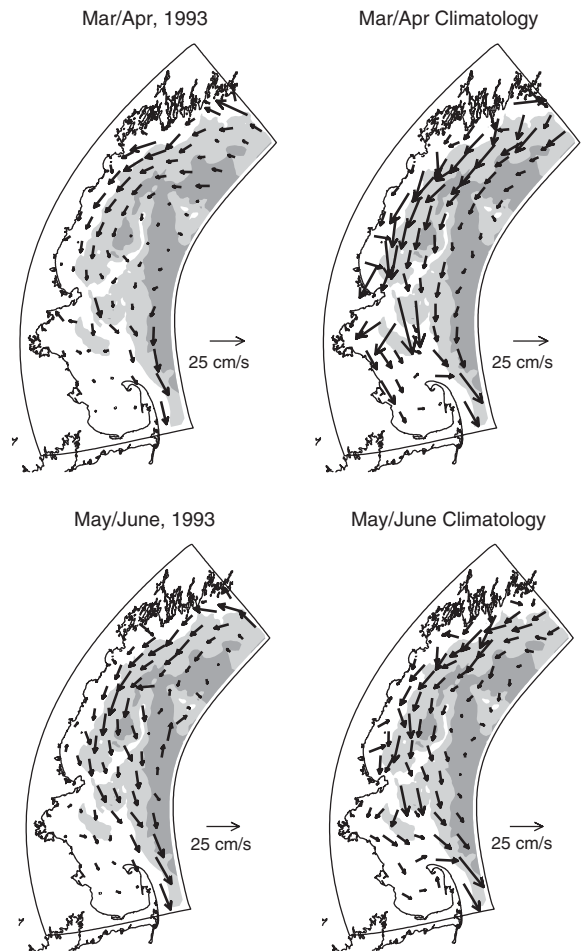


Fig. 7. Comparison of modeled mean surface currents from March 19–April 30 and May 1–June 6 (left panel) to the mean surface currents of the March/April and May/June climatology of Lynch et al. (1997). Depths contours are at 75 m and 150 m.

panel), with upwelling winds transporting fresh-water offshore (e.g., cruise 3) and downwelling winds pressing it against the coast (e.g. cruises 1 and 2). The modeled surface salinity is, on average, 0.7 psu greater than that observed. This may be due to either elevated mixing in the model, discrepancies in the initial conditions, or the failure to transport enough fresh water through the northern boundary. This discrepancy has little influence on *A. fundyense* growth (Fig. 4D) and has not compromised the transport within the coastal current (Fig. 6).

While not perfect, the level of hydrodynamic skill described above should be sufficient for the goals of the analysis: to evaluate the ability of the model to match the timing and magnitude of bloom events. It is accepted that imperfectly known forcing, initial

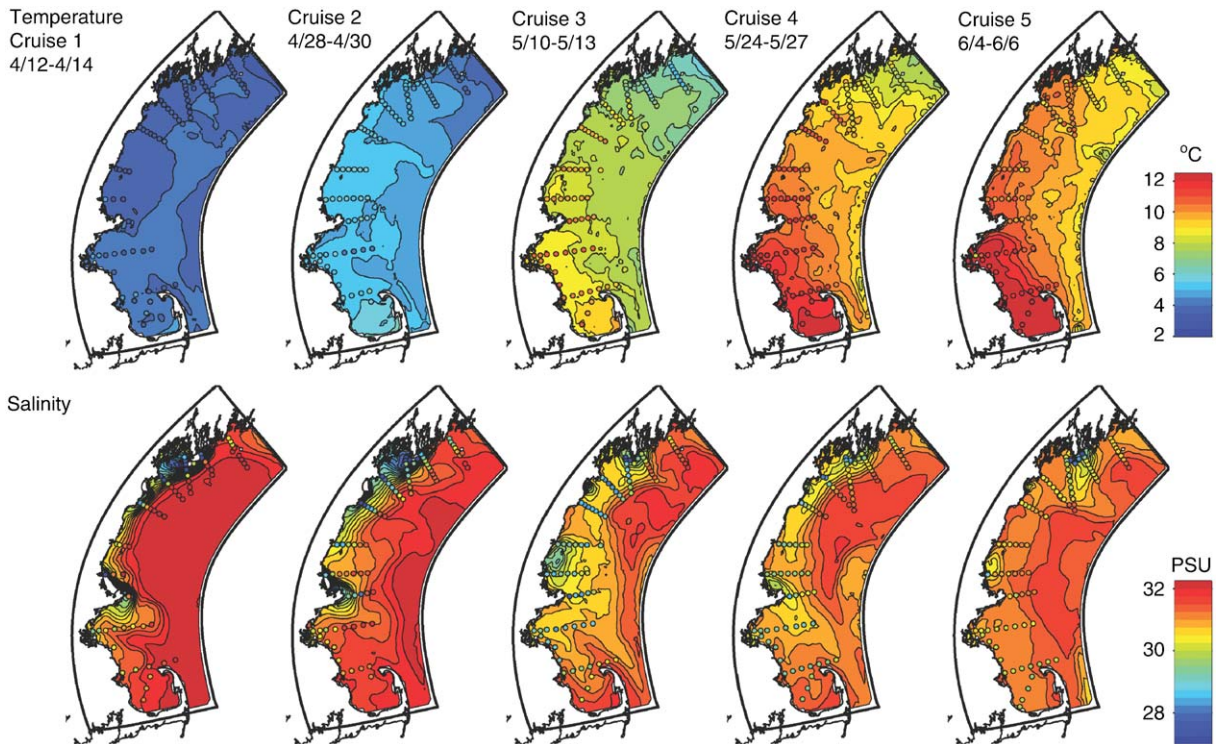


Fig. 8. Surface (2m) temperature and salinity comparison. Top panel: Modeled surface temperature (colored contours) versus observations (colored dots). The dots and contours are on the same color scale. Closely matching colors corresponds to a close model/data match. Bottom panel: Modeled surface salinity (colored contours) versus observations (colored dots).

and boundary conditions, energetic mesoscale circulations that cannot be deterministically simulated by the present forcing, and motions left unresolved by the present grid spacing will all contribute to the model/data misfit. Potential consequences of this will be discussed in detail below.

3.2. Biological model results

3.2.1. The baseline model

The best baseline model simulation is achieved by setting both μ_{\max} and d_g to the lower limits of their uncertainty ranges (Table 4). The resulting simulation captures the progressive rise in mean cell concentrations during the first three cruises, as well as the minimal cell concentrations in Massachusetts and Cape Cod Bays during the first two cruises (compare Figs. 9A, B). While much of the observed small-scale patchiness has not been captured (e.g., the failure to recreate 4 observations of 30–100 cells/C observed just outside of Casco Bay during cruise 1), these misfits alone are not inconsistent with the goal of simulating the timing and magnitude of the

observed bloom. However, the skill of the baseline model degrades from Cape Ann southward in the third cruise, and the model grossly over-estimates *A. fundyense* populations throughout the domain thereafter. This generates large misfits correlated over long spatial scales and a correspondingly low likelihood (Table 4).

3.2.2. Mortality only

When mortality (m) is added as a degree of freedom, the maximum likelihood result occurs at $m = 0.15 \text{ day}^{-1}$ (Table 4). Modeled *A. fundyense* concentrations in this case are similar to the baseline case during the first two cruises (compare Figs. 9B and C). However, unlike the baseline case, the modeled cell abundance no longer increases well beyond that observed during the last three cruises. This leads to a marked decrease in the misfit variance, its spatial and temporal scales, and a corresponding increase in the likelihood relative to the baseline model (Table 4). The significance of this improvement in fit is shown by comparison of values of the maximum likelihood for different choices of mortality (Fig. 10A). The overall

Table 4
Parameters of statistical model for the best run for each model structure

	Baseline	Mortality	Nutrients	Mortality + nutrients	Zero net growth
μ_{\max} (day ⁻¹)	0.460	0.525	0.460	0.575	NA
d_g (cm)	0.50	1.25	0.50	1.25	1.25
m (day ⁻¹)	0	0.15	0	0.1	NA
K_N (μM)	0	0	3.0	0.5	NA
$\log(L)$	-584.6	-568.7	-569.3	-567.7	-572.9
s^2 (raw sample variance)	7.10	2.49	2.55	2.34	2.63
σ^2 (fit by likelihood)	6.35	2.56	2.71	2.51	2.81
r_x (km ⁻¹)	0.0194	0.0534	0.0492	0.0541	0.0487
r_y (km ⁻¹)	0.0196	0.0566	0.0520	0.0566	0.0503
$\rho_{\Delta t=1}$	0.189	0.196	0.182	0.170	0.203
$\rho_{\Delta t=2}$	0.113	0.106	0.083	0.084	0.084

Note that two variance values are reported. The first is that associated with the 386 observed misfits. The second is that fit by maximum likelihood process. While the two are close in size, differences reflect the influence of space/time correlation and incomplete sampling. The variance of the *A. fundyense* observations is 2.60.

maximum for the mortality only structure ($m = 0.15 \text{ day}^{-1}$) serves as the likelihood of the alternative, “baseline and mortality” hypothesis (i.e. $\log(L_1) = -568.7$). The dashed and solid horizontal lines define the likelihood thresholds for the 90% and 99% confidence intervals around this best case. That is, for a given confidence interval, they identify the likelihood below which it is possible to reject null hypotheses stating specific values of m in favor of the best simulation. The hypothesized baseline model ($m = 0 \text{ day}^{-1}$) yields a maximum likelihood ($\log(L_0) = -584.6$) far below both thresholds, and it can thus be strongly rejected. This is also true at the 90% level for null hypotheses that claim specific values of $m \leq 0.05 \text{ day}^{-1}$, and those that claim specific values of $m \geq 0.025 \text{ day}^{-1}$. However, hypotheses claiming values of m within the clearly defined maximum between $m = 0.1 - 0.2 \text{ day}^{-1}$ are not distinguishable from the best simulation at the 90% level. The MLRT thus provides information necessary to reject the baseline model, and identifies a range of mortality values that produce statistically similar results.

3.2.3. Nutrients only

When K_N is added as a degree of freedom, the maximum likelihood simulation occurs with $K_N = 3.0 \mu\text{M}$ (Fig. 9D, Table 4), but values greater than $1.5 \mu\text{M}$ produce results that are statistically similar at the 90% level (Fig. 10B). As was the case with mortality, the baseline model structure can be strongly rejected based on its inability to control cell levels during the last two cruises of the field season. Clearly, some additional loss or limitation is

needed to reproduce the timing and magnitude of the bloom, but it is not yet clear if this is best provided by nitrogen limitation or mean mortality.

3.2.4. Mortality and nutrients

When both nutrients and mortality are included, the best simulation occurs at $K_N = 0.5 \mu\text{M}$ and $m = 0.1 \text{ day}^{-1}$ (Fig. 9E, Table 4). Consideration of this last model structure expands the one-dimensional likelihood analyses of Figs. 10A, B into a two-dimensional, “ K_N, m ” parameter space (Fig. 10C). The thick dashed and solid contours define the 90% and 99% confidence regions within the parameter space and are accordingly based on a χ^2 distribution with 2 degrees of freedom. The baseline model is located at the origin (circled). The points along the ordinate are those shown in Fig. 10A for the mortality only case, and those along the abscissa are those from the nutrients only case (Fig. 10B). The best simulations on each of these axes, along with the best overall, are circled. The confidence contours identify a broad band of parameter values that produce statistically similar results. The baseline model lies far outside of both regions, and can thus be strongly rejected. However, points associated with the nutrients only case and with the mortality only case lie within the 90% confidence region and cannot be rejected.

To understand the differences between the mortality only, nutrients only, and mortality and nutrients structures, closer inspection of the misfits during the last three cruises is needed (Fig. 9C–E). Two are particularly notable. First, the maximum likelihood run for all three model structures produce

cell populations in much of Massachusetts and Cape Cod Bays during cruise 3. *A. fundyense* is only observed in the immediate vicinity of Boston Harbor at this time (Fig. 9A). The magnitude of this misfit increases as mortality decreases (e.g., Fig. 9C versus D). The second notable misfit occurs offshore and to the North of Cape Ann during cruise 5. *A. fundyense* concentration highs are observed in Casco Bay and in Massachusetts Bay during cruise 4, and these high patches are well

connected by an intervening population at this time. However, the connecting population largely disappears in the observations by cruise 5. The simulations in Fig. 9C–E all reproduce the highs near Casco Bay and within Massachusetts Bay (although they are damped relative to the observations), but only those with nutrient dependence begin to capture the attenuation of the intervening population. This is due to the nearly complete depletion of nutrients within the intervening region

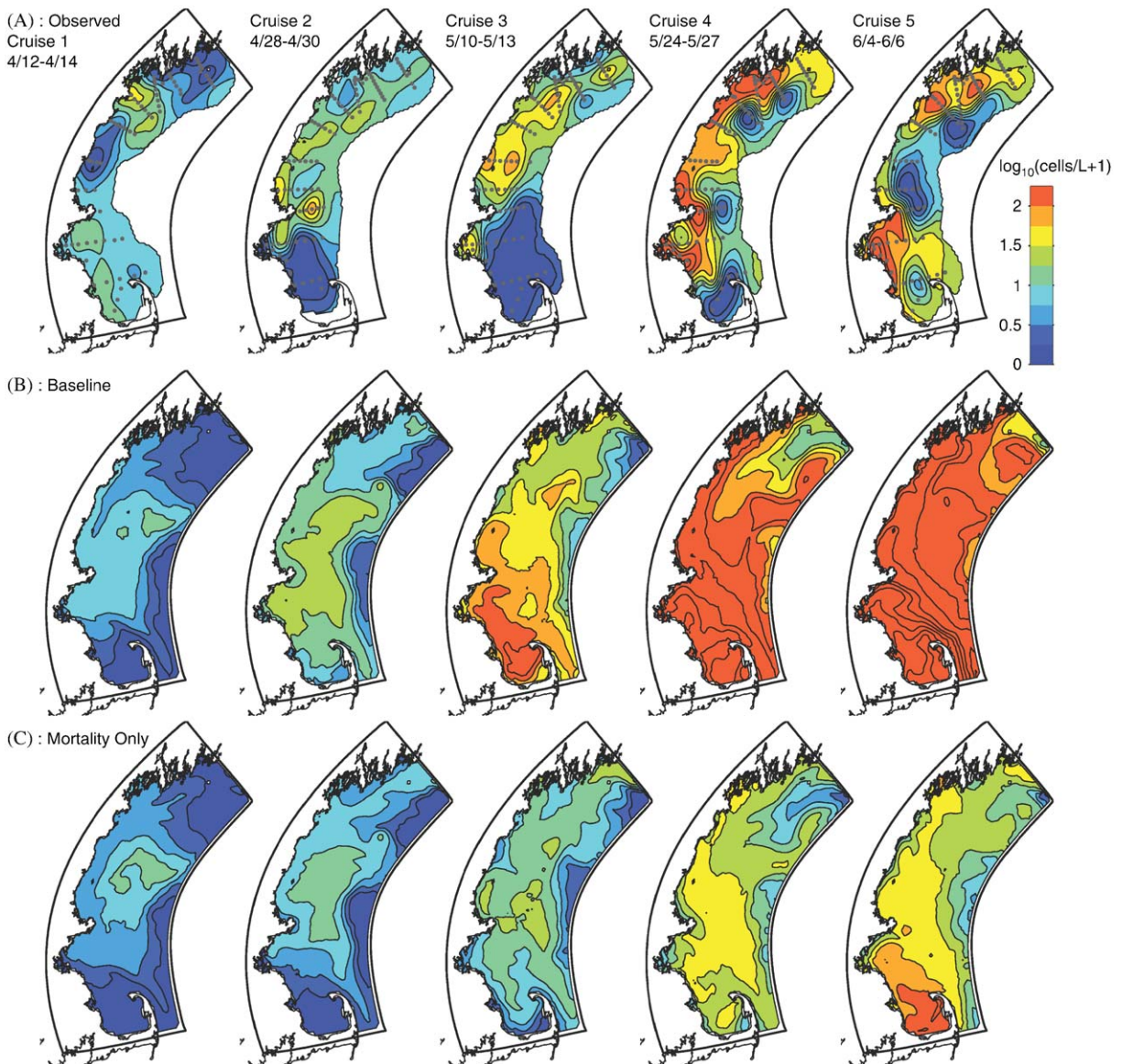


Fig. 9. Comparison of modeled and observed surface *A. fundyense* fields. Each horizontal panel corresponds to either observations or output from the simulations in Table 4, with each column corresponding to a cruise. Panels are as follows: (A) The observed *A. fundyense* distribution, (B) best baseline model, (C) best model with mortality only, (D) best model with nutrient dependence only, (E) best run with mortality and nutrient dependence (best overall), and (F) The best simulation with net growth set to 0 day^{-1} .

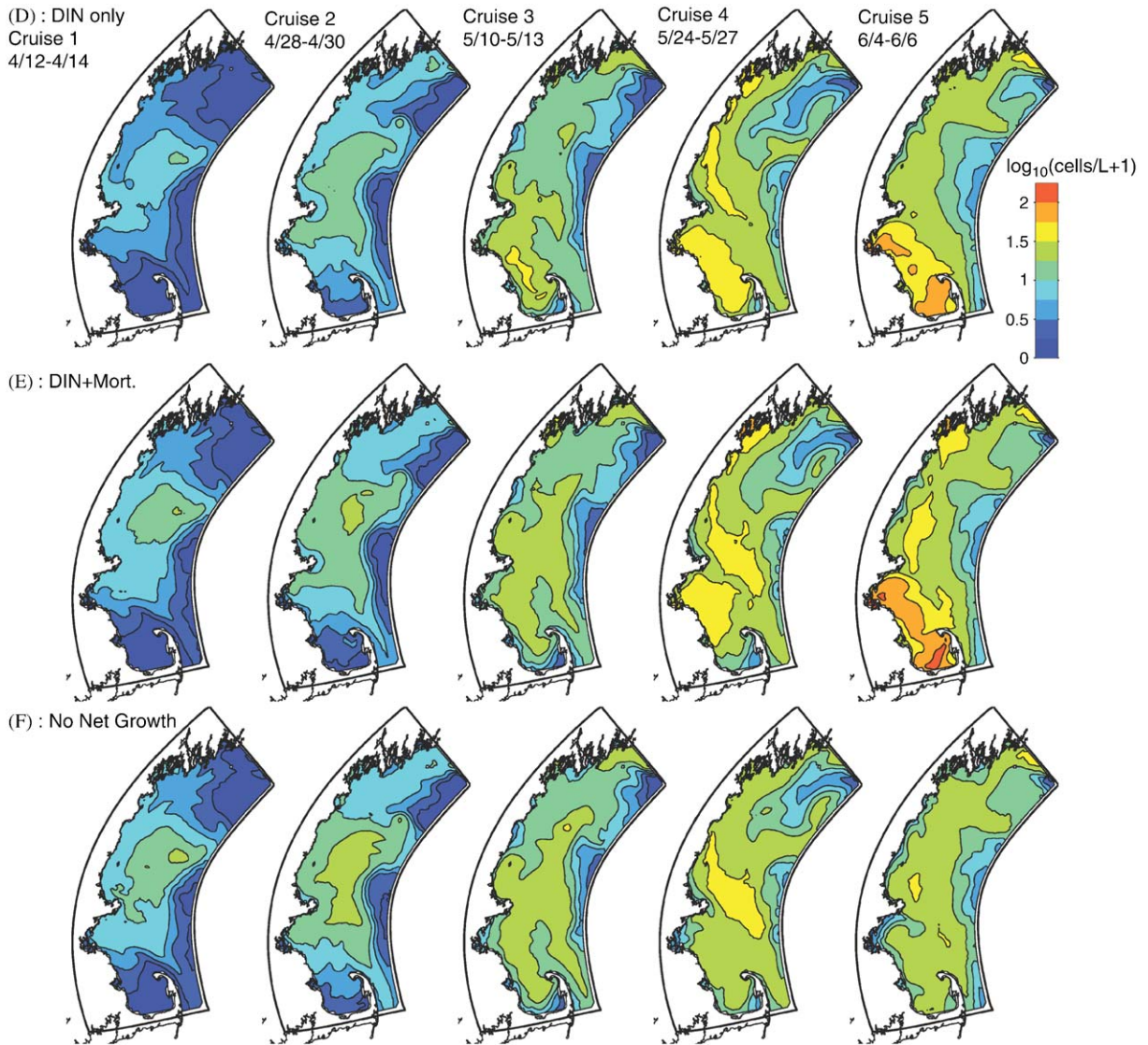


Fig. 9. (Continued)

by cruise 4 (see Fig. 2B). The optimal run has the most success in minimizing the combined effect of these two misfits: The moderate mortality rate (0.1 day^{-1}) controls the cell abundance in Massachusetts and Cape Cod Bays during cruise 3, while the combination of nitrogen dependence and mortality begins to recreate the attenuation of the *A. fundyense* population between Casco Bay and Massachusetts Bay from cruise 4 to 5. However, the increase in skill is not enough to confidently differentiate the maximum likelihood run using both mortality and nutrients from the best simulations using either mortality or nutrients.

3.2.5. Zero net growth

The best run imposing the condition of zero net growth (and optimizing over d_g only) is summarized in Table 4 and shown in Fig. 9F. This simulation introduces cells via germination and flow through the northern boundary, but cells are simply transported by the model circulation once within the domain. Although it is impossible to attach a precise level of significance to the change in fit between the best overall run and the zero net-growth case (see discussion in Section 2), there is a notable decrease in the likelihood and corresponding increase in the misfit variance for the latter.

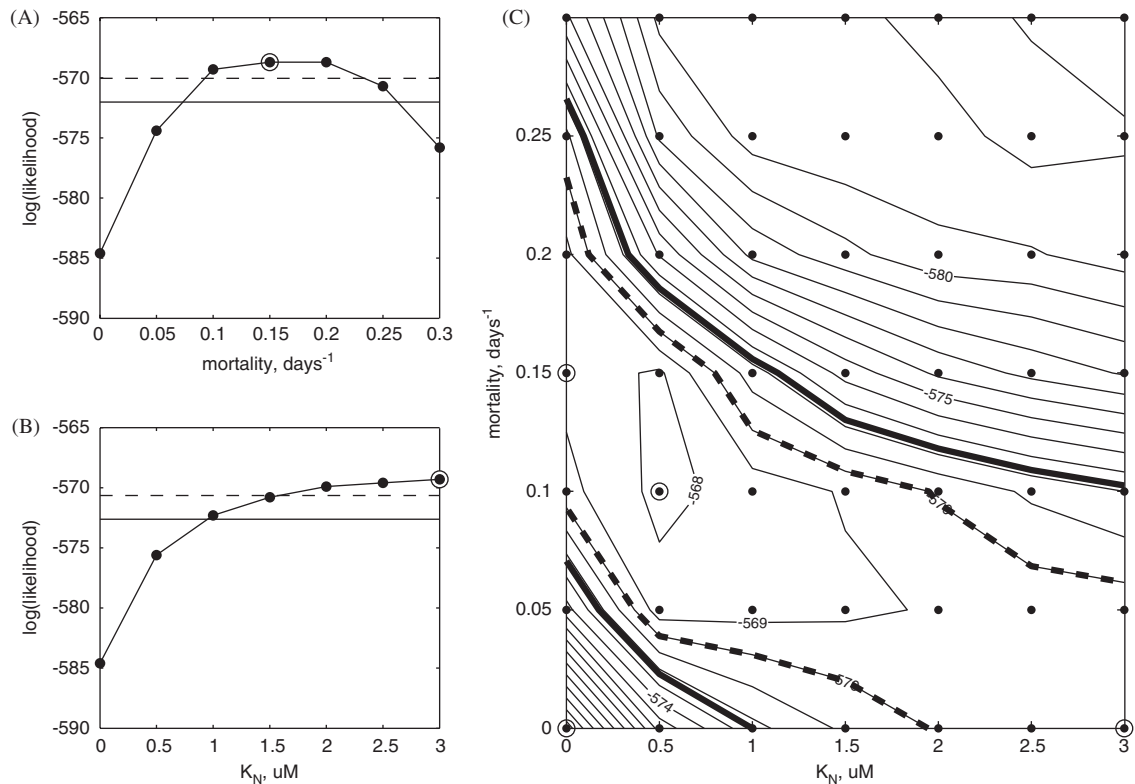


Fig. 10. The MLRT results. (A) Plot of maximum log-likelihood ($\log(L)$) for comparison of the mortality only structure to the baseline model structure. Dots signify values of m where the likelihood is maximized over d_g and μ_{\max} . The maximum likelihood over all m occurs at $m = 0.15 \text{ day}^{-1}$ (circled). The dashed horizontal line marks the 90% confidence threshold, the solid horizontal line marks the 99% confidence threshold. (B) Plot of maximum $\log(L)$ for comparison of the nutrients only model structure and the baseline case. Markings are the same as in (A). (C) Contours (interval = 1) of maximum $\log(L)$ as a function of K_N and m . The thick dashed line marks the border of the 90% confidence region. The thick solid line, marks the 99% confidence interval. The best simulation occurs at $K_N = 0.5 \mu\text{M}$, $m = 0.1 \text{ day}^{-1}$ (circled). The points along the ordinate are those from the mortality only model structure. Those along the abscissa are from the nutrient only model structure. Best simulations for each of these cases, as well as the baseline model (origin), are circled.

Comparison of the modeled fields reveals that the largest difference between the two simulations is the inability of the zero net growth case to create regions of increased abundance near Casco Bay and within Massachusetts Bay during the last two cruises. The best simulation also produces a bloom that is generally more constrained to coastal areas, as is suggested by the observations. However, it is notable that the zero net-growth simulation produces a bloom of approximately the right magnitude. Growth and mortality contribute to potentially important spatial features within the bloom, but they do not dramatically change the overall cell abundance.

3.3. Misfit model verification

Before ratifying the above analysis and moving onto model assessment and diagnosis, consistency

between the misfits produced by the model/data comparison and the proposed misfit model must be verified. Some asymmetry is apparent in the raw misfits associated with the best simulation (Fig. 11A), with a prevalence of over-estimation by the model. However, this histogram does not account for spatial and temporal covariance between the misfits. Inspection of Fig. 9E reveals several regions of persistent over-estimation (e.g., Cape Cod Bay during cruise 3). Misfits associated with the individual observations in these patches are not independent, but part of the same larger misfit. This can be accounted for by scaling the misfits according to $C_{\epsilon\epsilon}^{-1/2}\epsilon$, where $C_{\epsilon\epsilon}^{-1/2}$ is the Cholesky decomposition of the covariance matrix (Houseman et al., 2004). If the covariance description is appropriate, this multiplication will isolate the independent portions of the misfit and normalize them. The result (Fig. 11B) shows that the misfit

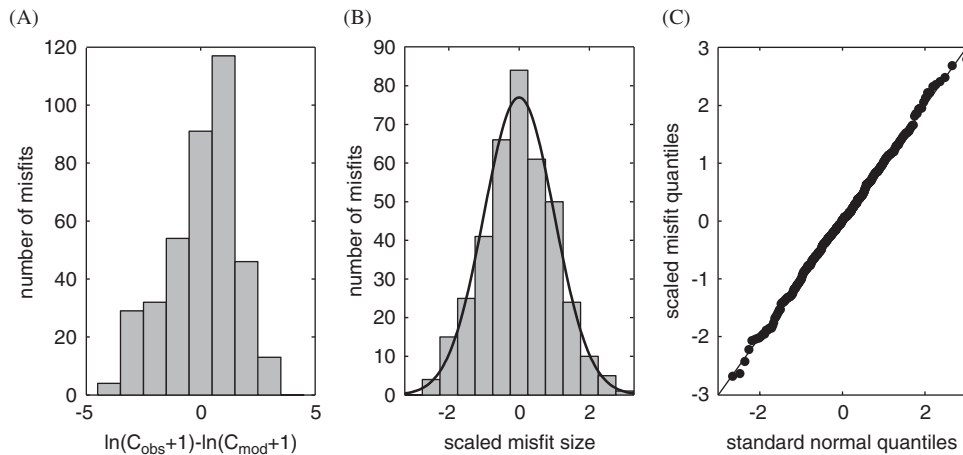


Fig. 11. Misfit model diagnostics: (A) The histogram of the misfits associated with the optimal simulation. (B) The misfits for the optimal simulation after scaling by the covariance matrix. If the statistical representation has adequately described the primary features of the model/data misfits, the scaled misfits will be normally distributed with mean 0 and a variance of 1 (solid line). (C) Quantile–Quantile plot of the scaled residuals. If the misfit model herein is accurate, the quantiles associated with the standard normal distribution will correspond with those of the sample and the plot of one against the other will follow a straight line with slope 1.

histogram adjusted for covariance is both symmetric and normal. Plotting the quantiles of the scaled misfits against standard normal quantiles and noting that they follow a straight line confirms this (Fig. 11C).²

Several additional diagnostic plots (Fig. 12) are necessary to ensure that a single, time and space invariant description of the misfit is appropriate and that the representation of the covariance (14) is adequate. Plotting the scaled misfit associated with the overall best simulation as a function of modeled concentration (Fig. 12A) reveals no large changes in the misfit properties at high or low model values. The time invariance (i.e. stationarity) of the misfit properties is supported by Fig. 12B, which plots the scaled misfits in the order in which the observations were collected. Lastly, the spatial decorrelation scales estimated via maximum likelihood theory are largely consistent with that suggested by a simple autocorrelation plot for the misfits (Fig. 12C, D).

²Quantiles are defined such that the f quantile of a data set is the value below which a fraction f of the data lies. The median of a data set is thus the 0.5 quantile. plotting the quantiles from the scaled misfit sample against those expected from a standard normal distribution thus provides a means to evaluate the normality of the scaled misfit sample. Curvature can indicate skew, abnormally long or short distribution tails, or asymmetry. Discussion of this residual diagnostic and others herein can be found in Draper and Smith (1981) and Cook and Weisberg (1982).

The estimated cross-shore decorrelation scale is slightly higher than the sample autocorrelation (Fig. 12D). Diagnosis (not shown) suggests that this primarily results from a limited number of more highly correlated misfits in the Massachusetts and Cape Cod Bay region. Aside from this suggestion of mild spatial heterogeneity, the representation of the spatial correlation decay (14) appears suitable. Furthermore, the combined results of Figs. 11 and 12 suggest that the choice of the misfit model and the implicit assumptions about the misfit weights associated with it are indeed reasonable.

3.4. Model assessment

Assessment of what has been resolved by the model is critical before diagnosis, as this largely determines the nature of the mechanistic questions that should be asked of the output. The graphical comparison of Fig. 9 suggests that the model has produced a smoothed version of the observations. Considerable misfits exist at individual points, but the seasonal progression of bloom magnitude from April to June appears to be in agreement. This serves as a first check of model plausibility, as it was unclear a priori if the model as formulated could produce *A. fundyense* cell populations remotely near the magnitude of those observed. In addition to this basic agreement, some of the first-order observed space–time variability within cruises is also apparent in the model, such as the high

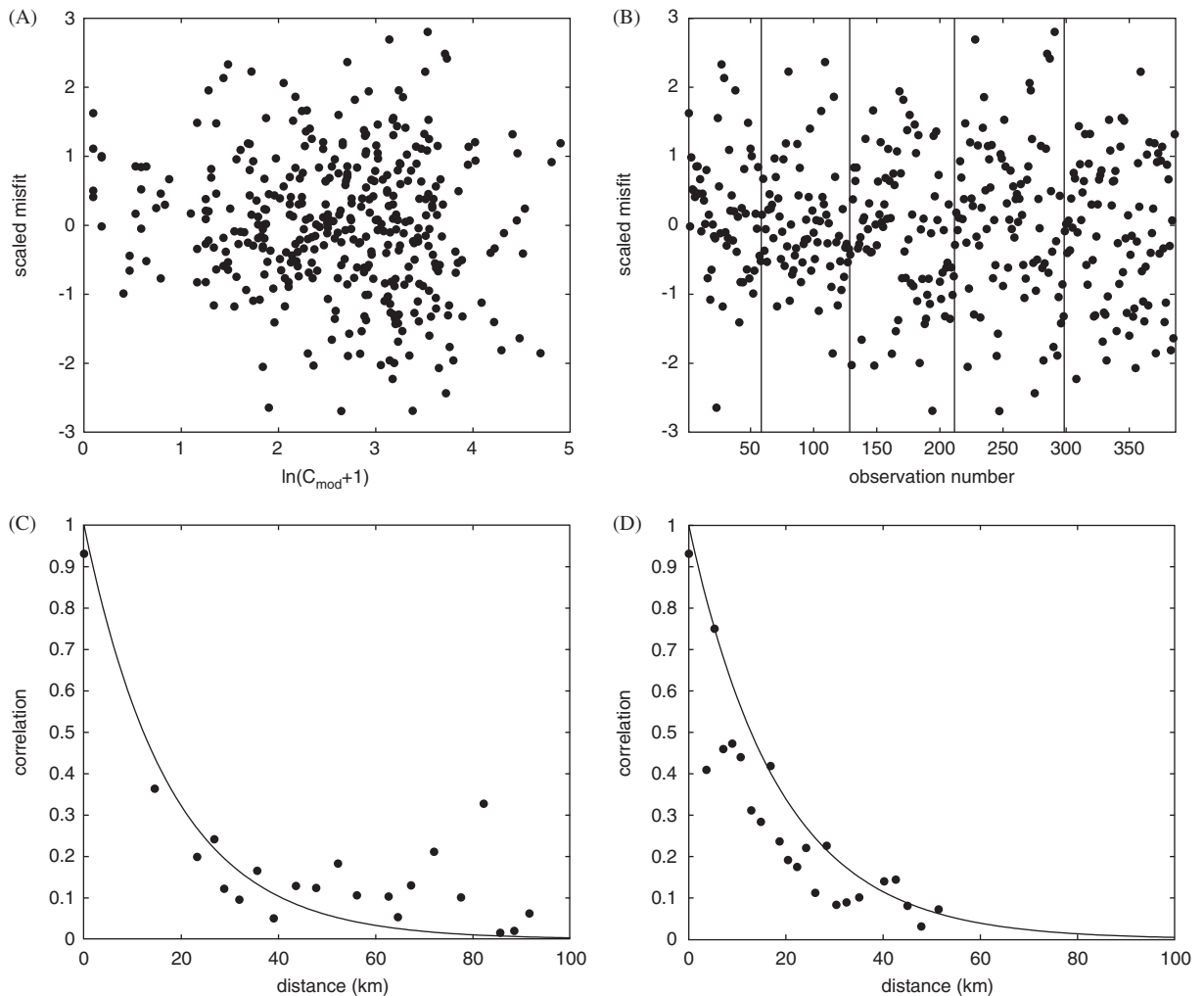


Fig. 12. Misfit model diagnostics: (A) Plot of the scaled misfit versus the log of the model estimate to test for systematic departures between the model and the data over the range of the modeled abundance. (B) Plot of the scaled misfit versus the order in which the observations were taken to assess the stationarity of the misfit properties. Vertical lines delineate the boundaries between different cruises (cruise 1 = 1–58, cruise 2 = 59–128, cruise 3 = 129–211, cruise 4 = 212–298, cruise 5 = 299–386). (C) Plot of the spatial autocorrelation of the data for points oriented in the along-shore direction ($\pm 0\text{--}30^\circ$ angle from purely along-shore, \bullet) and the along-shore decay estimated by m.l.e. (black line $r_y = -0.0566 \text{ km}^{-1}$). (D) Plot of the misfit spatial autocorrelation for points oriented in the cross-shore direction ($\pm 30^\circ\text{--}90^\circ$ from purely along-shore, \bullet) and the cross-shore decay estimated by the m.l.e. (black line, $r_x = -0.0541 \text{ km}^{-1}$).

A. fundyense concentrations within Massachusetts Bay and near Casco Bay.

Despite the promise of the qualitative comparison, the raw misfit correlation coefficient (r) and coefficient of determination (r^2) for the best simulation are a humbling 0.32 and 0.10. This is partly due to the smoothed model representation of the observed bloom (see above), but a second explanation derives from the fact that most of the variance in the data occurs over patch scales of 10–30 km. Relatively modest patch displacements in the model will thus lead to large misfit variances. Displace-

ments of this scale could have a myriad of origins, but one likely source is energetic mesoscale meanders and eddies within the coastal current (see discussion in Churchill et al., 2005). These motions exist in the present physical model (grid spacing of 1.5–3 km) but cannot be deterministically replicated without more detailed knowledge of the forcing. Such motions are deemed responsible for substantial point-to-point misfits in hydrographic properties within a similar simulation of the Gulf of Maine circulation to that used herein (Hetland and Signell, 2005). Since *A. fundyense* is advected by these same

physical dynamics, substantial point-to-point misfits are likely even for a perfect biological model.

To quantitatively assess the model's ability to capture broader patterns in the *A. fundyense* distribution and abundance, the log-transformed model output and the data are averaged over a range of spatial scales (Table 5). The model shows strong correlation with the data when averaged on a cruise-by-cruise basis, and moderate correlation over scales > 50 km (approximately 1/5 the length of the domain). Below 50 km, correlations are weak and begin to approach that of the point-to-point comparison. Removal of cruise 3 from the comparison, which has been identified as containing several more prominent misfits, increases the skill considerably, particularly at the scale of the Cape Cod and Massachusetts Bay (50–100 km). This analysis supports the qualitative assessment above. Model skill is limited over small scales (<25 km) and model diagnosis should avoid questions that depend critically on dynamics at these scales. Fortunately, the questions of interest to this study: identification of the primary source of *A. fundyense* cells to the WGOM and the primary factors controlling bloom development, are best addressed on larger scales where the model shows considerable skill.

3.5. Model diagnosis

Diagnosis focuses primarily on inspection of *A. fundyense* fluxes and cell inventories within the domain (Fig. 13) and factors limiting net growth (Fig. 14). Diagnosis is not limited to the optimal simulation but includes the best simulations from the mortality only, nutrients only, and mortality

and nutrients cases (Table 4). These simulations are representative of the range of results within the 90% confidence interval of Fig. 10C. The results from the zero net growth case are also included in Fig. 13, as they provide a useful comparison.

The germination of offshore cysts (those lying in waters of > 50 m in depth) provides the largest flux of new *A. fundyense* cells to the domain throughout the first half of all the representative simulations (Fig. 13, panels A–D), and remains important throughout. The total flux from inshore cysts is only 7% that of those offshore for all three simulations. The introduction of new cells due to net growth (growth—mortality, panel C) is notable yet not dominant, as it accounts for 10–46% of the total new cell flux during the simulation period. It becomes more prominent toward the end of the simulations, particularly for those models with weak or no nutrient dependence. The flux of cells through the northern boundary accounts for just 7–11% of new cells introduced to the domain during the simulation period. However, over the last month of the simulation this flux reaches 19–38% of that produced by cysts within the domain.

Panels E and F show that the increase in the transport of cells from the EGOM results from both an increase in cell concentration along the boundary and an increase in the tendency of the current to flow to the southwest. The mean current transporting *A. fundyense* into the domain through the northern boundary in March and April is 4.1 cm s^{-1} , while it reaches 6.1 cm s^{-1} in May and June. This occurs despite the increased prevalence of upwelling favorable winds in May/June, which periodically interrupts the southwest surface flow,

Table 5

Comparison of the sample correlation (r) and the sample coefficient of determination^a (r^2) for comparisons of the model and the data (after log transform) averaged over different spatial scales

Averaging scheme	Variance of observations (after averaging)	Variance of misfits (after averaging)	(r/r^2) All Cruises	(r/r^2) No Cruise 3
Cruise by cruise	0.39	0.13	0.82/0.68	0.88/0.77
100 km scales	0.44	0.23	0.70/0.49	0.85/0.72
50 km scales	0.79	0.54	0.56/0.31	0.72/0.52
25 km scales	1.36	1.04	0.48/0.23	0.59/0.35
10 km scales	1.98	1.64	0.42/0.17	0.51/0.26
Point-to-Point	2.60	2.34	0.32/0.10	0.41/0.17

For the cruise-by-cruise comparison, the mean of all the model values at the sample points is compared with the mean of all the observations for each cruise. For the spatial comparisons, all observations within a radius of the specified scale around each observation were averaged and compared with the mean modeled surface concentration over the same region.

^a $r^2 = 1 - \text{var}(\text{misfits})/\text{var}(\text{observations})$.

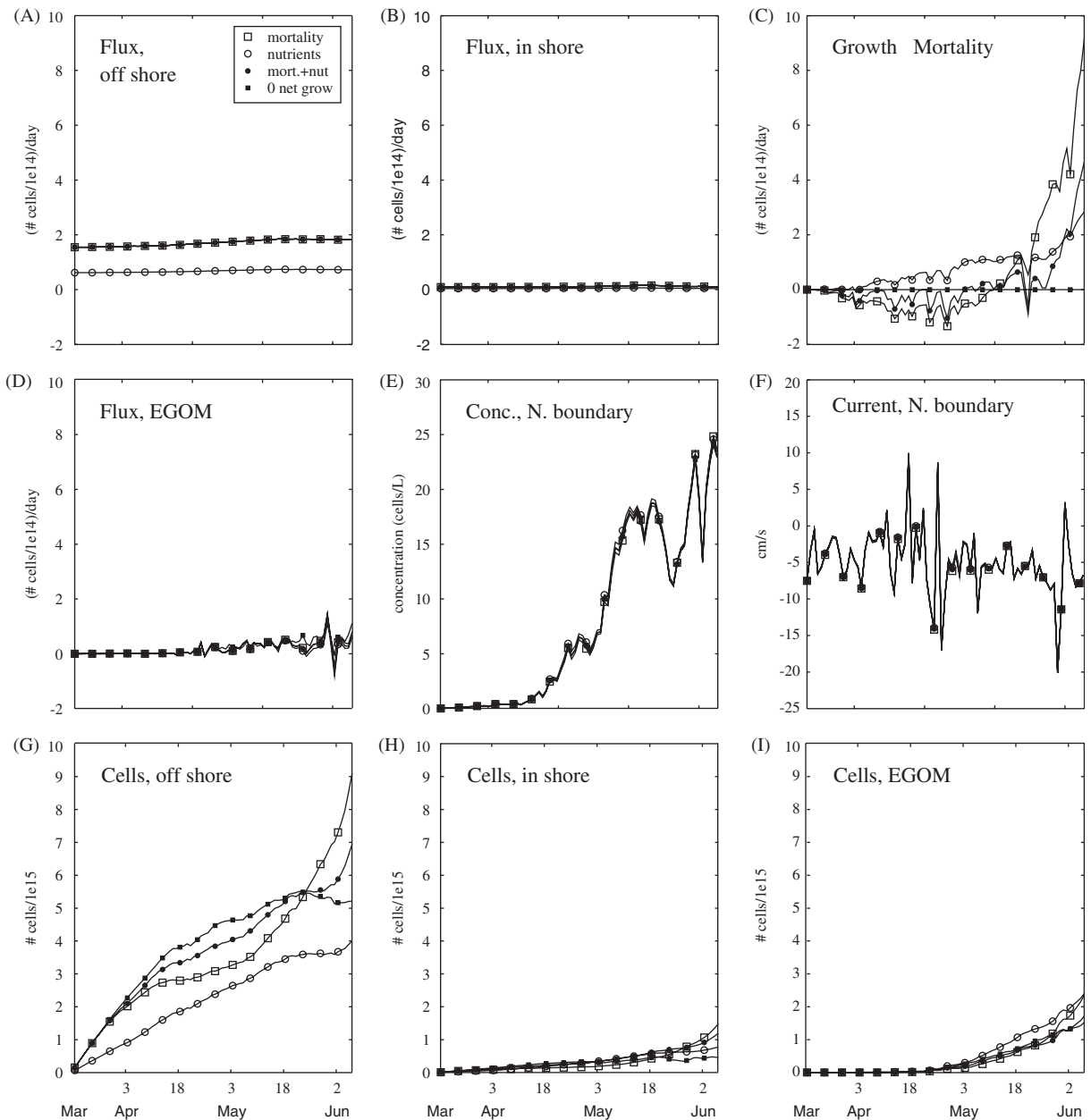


Fig. 13. The cell budget. Cell fluxes and inventories are tracked from various sources for each of the last four runs in Table 4. Panels are as follows, (A) Flux of newly germinated cells from off-shore (> 50 m deep) cyst beds. Note that mortality only, mortality and nutrients, and zero net growth have equal germination depths and thus overlap. (B) Flux of newly germinated cells from in-shore (< 50 m) cyst beds. (C) New cells produced via net growth. (D) Flux of cells through the northern boundary, presumably from the EGOM. (E) Mean concentration along the northern boundary (over the top 10 m) (F) The current velocity across the northern boundary. Negative values are into the domain. (G) The total number of cells within the domain that originated from offshore cysts. (H) The total number of cells in the domain that originated from inshore cysts. (I) The total number of cells that originated from the EGOM (north boundary).

pushing cells within the domain out the northern boundary (note the coincidence of outward velocities and sharp perturbation in the mean cell concentration with upwelling winds in Fig. 3, this is most apparent during the episode from June 2 to

3). This increased tendency for southwest flow in May and June relative to March and April is present in the climatology (Lynch et al., 1997), where it is caused by the spreading of dense slope water from Jordan to Wilkinson Basin. The concurrent increase

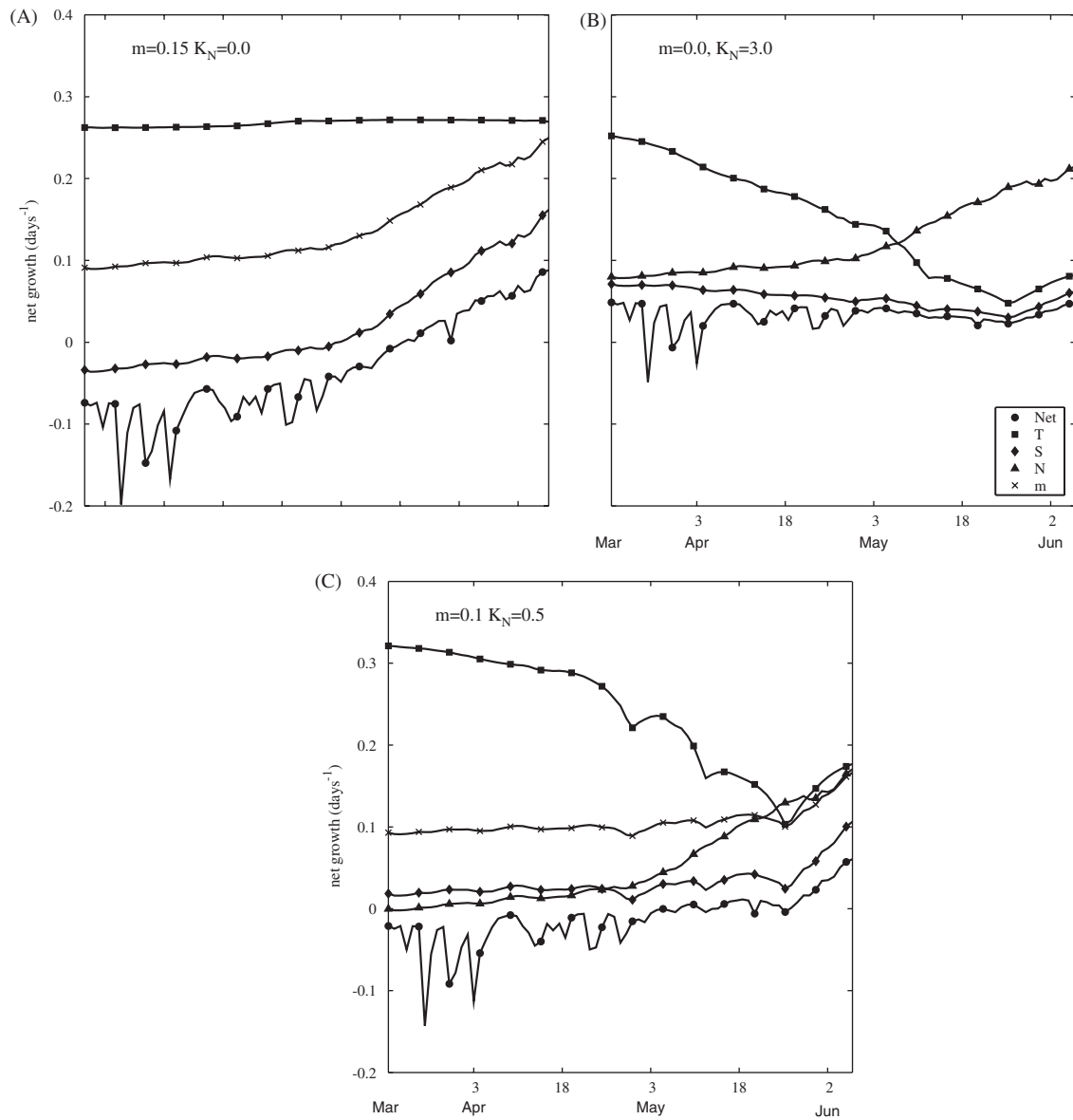


Fig. 14. Net growth analysis. Panels correspond to simulations in columns 2–4 of Table 4 (marked in upper left corner of each plot). The line marked with closed circles is the actual domain averaged net growth. Other lines correspond to what the domain averaged net growth would be with light at saturation and one other growth-influencing factor removed. Factors are T = temperature, S = salinity, N = nutrients (DIN), and m = mortality.

in cell abundances along the northern boundary (panel E) is consistent with a delayed peak in toxicity in the EGOM relative to the WGOM (Anderson, 1997). The peak cell concentrations observed in the EGOM in the summer months are generally much greater than those observed in the WGOM (Townsend et al., 2001). Thus, although wind patterns influence the modeled import of cells from the EGOM over short time scales, patterns in *A. fundyense* abundance and the climatological

circulation suggests that transport of cells from the EGOM becomes increasingly important to toxic outbreaks in the WGOM as spring progresses into summer.

The overall importance of *A. fundyense* cells originating from different potential sources is a function of both the flux of new cells into the model domain, and subsequent net growth within the domain. Cells originating from offshore cystbeds, inshore cystbeds, and flow from the EGOM were

therefore tracked as separate populations (Fig. 13, panels G–I). Cells originating from offshore cysts are most prominent, accounting for 72–83% of the average cell abundance³ during the simulation. Cells originating from inshore cystbeds and cells originating in the EGOM account for 7–10% and 8–18%, respectively. These contributions increase to 10–11% and 17–32% over the last week of the simulation. Comparison of the best-fit and zero net growth cases reveal little change in the total cell number. In general, changes via net growth are limited to a factor of 2 difference for all parameter settings within the 90% confidence interval of Fig. 10C (not shown).

Comparison of the modeled domain-averaged net growth rate to what the rate would be with light at saturation intensity and one additional growth-influencing factor removed (Fig. 14) suggests prominent roles of temperature, nutrient limitation, and mortality in limiting the net-growth of cells within the domain. Light only imposes a significant limitation during sporadic cloudy days, primarily at the beginning of the run (note the sharp downward spikes in net growth in late March and early April). Removal of this signal allows focus on longer time-scale trends that evolve over the bloom season. Temperature is the predominant factor slowing the realized net growth until early May for all the simulations. In early May, the temperature rises rapidly (Fig. 8), DIN concentrations drop (Fig. 2b) and, in all cases except the mortality only run, nutrients begin to play a more prominent role in limiting the realizable net growth. That is, if the influence of temperature were removed late in the simulation, nutrient limitation would still prevent net growth rates from increasing sharply. In the case of mortality—only run, the lack of nutrient dependence causes temperature and mortality to remain prominent factors in the limitation of realizable net growth throughout the simulation. The resulting domain-averaged realized net growth remains low ($<0.05 \text{ day}^{-1}$) throughout most of the run duration for all three simulations. This low net growth accounts for the considerable similarity between Fig. 10C–E and Fig. 10F (the zero net growth case), while spatial variability in the net

growth rate accounts for the notable differences in the simulated fields near Casco Bay and within Massachusetts Bay.

4. Discussion

4.1. Bloom initiation

The results described above have provided further insight into the initiation of *A. fundyense* blooms in the WGOM and the factors controlling bloom development. Regarding bloom initiation, the synthesis of what is known of the cyst distribution and germination rates provided herein suggests that cyst germination in the large cyst bed offshore of Casco Bay can account for the majority of the observed *A. fundyense* in the WGOM through early June of 1993. This is enhanced significantly by inflow from the EGOM, particularly late in the simulation. Germination from cysts in the shallow waters within Casco Bay contributes a small amount of cells relative to these other two sources. These results are notable relative to other studies (Keafer et al., 2005; Luerssen et al., 2005), which emphasize the linkage between shellfish toxicity in the WGOM (particularly near Casco Bay) and the inflow of cells from the EGOM. The importance of this linkage is supported, but it is also suggested that sources of cells within the WGOM play an important role in bloom development during the spring and should therefore not be discounted.

The primary uncertainties in the germination-driven source in the WGOM are the effect of sediment mixing on the ability of a cyst to germinate and gain the water column, and inter-annual variability in the cyst abundance (see additional discussion in Anderson et al., 2005b; McGillicuddy et al., 2005). The first of these uncertainties is parameterized herein using the sediment mixing parameter d_g (the germination depth). The addition of a sediment dynamics model (e.g., Shull, 2001) may provide the means of refining this simple representation. However, the complexity of the sediment dynamics involved (Wheatcroft and Martin, 1996), and connecting these processes to cyst germination makes this a formidable challenge. Greater understanding of inter-annual variability in the cyst abundance requires sustained efforts to map the cyst distribution over both yearly and decadal time scales.

Uncertainties in the influx of *A. fundyense* cells from the EGOM include inter-annual variability in

³Calculated as $\sum_{i=1}^n A_i^{\text{off}} / \sum_{i=1}^n A_i^{\text{tot}}$, where A_i^{off} is abundance of *A. fundyense* cells after i days originating from offshore cysts, A_i^{tot} is the total *A. fundyense* abundance after i days, and n is the number of days in the simulation. Other percentages of the cell abundance are calculated in a similar fashion.

flow patterns at the Penobscot bay branch point (Pettigrew et al., 2005) and limited constraint of the *A. fundyense* cell concentration and physical properties along the boundaries. The model matches observed concentrations along the northern-most transect fairly well by relying on the climatological mean flow and extrapolation of concentrations for the northernmost transect to the northern boundary (Fig. 9). However, this approach cannot capture the wind-driven barotropic pressure response along the boundary, which likely drives additional space/time variability in the influx. There is also a possibility that high concentrations along the northern boundary or along parts of the eastern boundary subject to inflows were missed by the temporal and spatial resolution of the surveys. Sensitivity tests suggest that extrapolating the values from the northern boundary over the first 20 grid cells of the eastern boundary would lead to an inflow of cells accounting for 13–28% of the cell abundance when averaged over the entire simulation, and 24–43% of the cell abundance when averaged over the last week (compared with 8–18% and 17–32% in Section 3). The analyses herein thus provide an initial estimate of the contribution of flow from the EGOM through June of 1993, but additional observations and a more complete representation of the physical dynamics along the domain boundary will further refine this estimate. These issues are the subject of ongoing study (He et al., in press).

4.2. Factors controlling the net growth of the bloom

Mean simulated net growth rates were generally modest ($<0.05 \text{ day}^{-1}$) in those runs capable of recreating the timing and magnitude of the observed bloom. Net growth was thus a notable, yet non-dominant determinant of the *A. fundyense* cell distribution and bloom magnitude. The statistical analysis identifies the need for either mortality or nutrient limitation to match the observed bloom timing and magnitude, but cannot strongly differentiate between simulations using a wide range of these two factors. Other studies also suggest that both of these processes may be important. In the case of nutrient dependence, Poulton et al. (2005) observed trends in *A. fundyense* toxin composition in the WGOM that were consistent with nitrogen stress late in the spring. McGillicuddy et al. (2005), using a similar set of biological models to those herein within a Gulf-wide domain, found that excluding nutrient dependence led to rapid bloom

growth in the summer months. This resulted in an unreasonably large July and August *A. fundyense* abundance in the WGOM relative to typical observed concentrations. It is therefore notable that the mortality case herein shows particularly strong positive net growth (Fig. 14) and a notable increase in *A. fundyense* abundance (Figs. 9C, 13) at the end of the simulation (early June); a trend consistent with the results of the Gulf-wide analysis.

Studies of zooplankton grazing carried out in the region (Teegarden et al., 2001; Cambell et al., 2005; Turner and Borkman, 2005) suggest that common mesozooplankton species may be a significant source of mortality for *A. fundyense*. Many of the grazers tested in these studies did not selectively avoid toxic *A. fundyense* when it was present in the low concentrations common to the WGOM. Estimates of the grazing impact were highly variable and generally linked to fluctuations in in situ grazer abundance. Increased understanding of fluctuations in grazer abundance and more complete resolution of the community grazing response (including micro-zooplankton) would yield better resolution of the mortality term herein. The potential linkage of encystment with nutrient stress (Anderson et al., 1984) may also create spatial/temporal variability in the loss term, and investigation of thresholds and rates for this process is needed.

There are thus several concurrent studies that support the inclusion of both mortality and nutrient dependence in the model. However, like the model/data comparison herein, they are limited in their ability to constrain the relative importance of one versus the other. It is therefore critical that a range of simulations from within the confidence interval in Fig. 10C be considered if robust results are to be identified. Simulations within this range differ not only in the relative importance placed on mortality and nutrient dependence, but also in other aspects of the source and growth dynamics (i.e. Table 4). Simulations with a high dependence on mortality generally call for larger germination sources and high maximum growth rate, while those relying solely on nutrients invoke a smaller source and a lower maximum growth rate. They thus span a range of proposed source and development dynamics capable of explaining the primary observed features of spring *A. fundyense* blooms in the WGOM.

Application of the model with the exact tuned parameters herein to other regions and times should be approached with caution. The results of

McGillicuddy et al. (2005) suggest that, in addition to capturing observed patterns within the WGOM in 1993, the model also can capture mean seasonal patterns within the Gulf of Maine. However, several of the parameters within this model (most notably m) represent the influence of multiple processes (i.e. grazing pressure, cell death, and encystment) and have been derived based on the net effect of those processes within the WGOM in 1993. They are thus not inherent properties of *A. fundyense*, but properties of an *A. fundyense* bloom within a specific environment. The model framework should thus be re-optimized when applied in different regions, particularly if it is suspected that the dynamics underlying these parameters (e.g., the zooplankton community, the nutrient environment) are drastically different than those within the WGOM. Such an effort also may yield better constraints depending upon the quality and quantity of the observations available and the properties of the region under study. The incorporation of more advanced optimization techniques such as the adjoint method (Lawson et al., 1995, 1996; McGillicuddy et al., 1998) may ease the computational cost of such re-optimization.

4.3. Future model improvement and remaining misfits

Improvement to the biological model presented herein is made difficult, not just due to the challenge of parameterizing increasingly complex biological processes, but also due to difficulty detecting changes in the model/data fit that result from biological improvements. This is particularly true when the model/data comparison serves as a primary means of constraining biological model parameters (as it does herein). Utility in this regard can be confounded by limited spatial/temporal coverage and uncertainty in the observations, or by errors in the physical simulation that are reflected in the biological misfit.

Logical starting points when considering future model improvement include the largest remaining dynamical uncertainties (discussed above) as well as the remaining model/data misfits. One of the more prominent misfits identified in this study was the model over-estimation of the cell abundance within much of Cape Cod and Massachusetts Bays during cruise 3. Analysis (not shown) reveals that much of the increase in *A. fundyense* abundance in this region between cruises 2 and 3 is due to positive net growth. With this in mind, it is notable that the

period between the cruises covers a sharp transition in the factors influencing net growth: the temperature increases, a strong thermocline develops, and nutrient concentrations decrease rapidly. The simplifying assumptions of the biological model (e.g., constant mortality) are perhaps most questionable during this period. Increased spatial/temporal resolution of mortality dynamics thus offers one possible means to attenuate the model/data misfit in the region. Alternatively, the tendency for the model to overestimate the observed velocity at Cape Porpoise may be the root of this misfit. If the tendency for overestimation is persistent over the region between Casco Bay and Cape Ann, it would decrease the mean travel time between the regions (~100 km apart) from ~9 to ~7 days. This could potentially lead to an early introduction of cells to Massachusetts Bay within the model. Once within the region, any initial misfit may be enhanced by subsequent growth dynamics.

The physical/biological indeterminacy of the misfit origin is exacerbated at smaller spatial scales (~15–25 km) where mesoscale circulations not deterministically replicated by the model can produce displacements of similar length scale to the *A. fundyense* patches themselves. As mentioned previously, this suggests that even a perfect biological model would have considerable misfits when compared with data on a point-to-point basis in this setting. The dominance of misfits at this small scale further implies diminishing improvements in the model/data comparison from continued increases in the complexity in the biological model. This will limit the ability of the model/data comparison to differentiate between model structures and constrain additional parameters. Increased study of the influence of the physical simulation on the model/data fit is needed to better understand and minimize these limitations. This ultimately may be best addressed by incorporating physical uncertainty directly into optimization procedure.

Physical uncertainty can be decreased either through more direct observation of the forcing elements, or through the assimilation of current data to infer forcing. Assimilation strategies have been implemented successfully to improve circulation model performance in coastal regions (Lynch and Naimie (2002) provide an overview of recent efforts). However, success is contingent upon the availability of relevant observations (current, pressure, etc.) for assimilation. The current national emphasis on coastal observations systems (Clark

and Isern, 2003) will certainly improve future capabilities: of course, in retrospective studies, observations are likely to be sparse by present and future standards.

5. Conclusions

The findings of this study are largely consistent with the WGOM bloom dynamics outlined by Franks and Anderson (1992a) and in subsequent refinements (Anderson et al., 2005a). However, quantitative analysis of the 1993 RMRP data within the context of a coupled physical–biological model has provided many additional insights. Simulations suggest that cysts germinated from beds offshore of Casco Bay are capable of providing the majority of cells needed to account for the observed timing and magnitude of *A. fundyense* blooms in the WGOM during the spring. Cells from inshore cysts play a relatively minor role, although contributions may be significant locally. As the spring progresses into summer, the EGOM source increases in importance due to the climatological tendency toward along-shore flow in May/June at the Penobscot Bay branch point and increasing cell levels in the EGOM. The average net *A. fundyense* growth rate is low, being first limited by low sea surface temperatures, and then by a combination of depleted nutrients and mortality. The model/data comparison was unable to determine the relative importance of these latter two factors. Overall, augmentation of the modeled cell abundance via net growth was modest, strongly linking the bloom magnitude to the size of the sources to the north. This is consistent with the southward transport of established populations hypothesized by Franks and Anderson (1992a). However, despite the fact that the domain-averaged net growth was low, simulations suggest that growth processes do create important spatial/temporal features within the bloom, including elevated concentrations near Casco Bay and Massachusetts Bay later in the simulation. Such features may be an important source of variability in the predominantly along-shore progression of toxicity in the WGOM.

Acknowledgements

We gratefully acknowledge the support of the US ECOHAB Program sponsored by NOAA, NSF, EPA, NASA and ONR. Stock also gratefully acknowledges the support of EPA STAR fellowship

(#91574901). We would like to thank Dan Lynch for his comments on early drafts and resulting discussions that we feel have greatly improved this work. Rich Signell for providing the physical model simulation and for his comments and suggestions. John Cullen for his suggestions regarding the growth model formulation. John Cullen, Stacey Etheridge, Bruce Keafer, Amy Bronzino, and Paty Matrai for their generous sharing of *A. fundyense* growth and germination data. Theodore Loder for providing the nutrient data, and Ruoying He for his suggestions that helped improve the physical simulation. We would also like to thank our ECOHAB colleagues for their valuable input throughout this effort. Lastly, we would like to acknowledge the valuable comments and suggestions of two reviewers, which were greatly appreciated and lead to notable improvements to this work.

This is WHOI contribution 11348, and US ECOHAB contribution 157.

Correspondence and requests for materials to Charles A. Stock (cstock@whoi.edu)

References

- Anderson, D.M., 1980. Effects of temperature conditioning on development and germination of *Gonyaulax tamarensis* (Dinophyceae) hypnozygotes. *Journal of Phycology* 16 (2), 166–172.
- Anderson, D.M., 1997. Bloom dynamics of toxic *Alexandrium* species in coastal waters. *Limnology and Oceanography Part 2* 42 (5), 1009–1022.
- Anderson, D.M., 1998. Physiology and bloom dynamics of toxic *Alexandrium* species, with emphasis on life cycle transitions. In: Anderson, D.M., Cembella, A.D., Hallegraeff, G.M. (Eds.), *Physiological Ecology of Harmful Algal Blooms*. Springer, Berlin, pp. 29–48.
- Anderson, D.M., Keafer, B.A., 1987. The endogenous annual clock in the toxic dinoflagellate *Alexandrium tamarensis*. *Nature* 325 (6105), 616–617.
- Anderson, D.M., Lindquist, N.L., 1985. Time-course measurements of phosphorous depletion and cyst formation in the dinoflagellate *Gonyaulax tamarensis* Lebour. *Journal of Experimental Marine Biology and Ecology* 86 (1), 1–13.
- Anderson, D.M., Stolzenbach, K.D., 1985. Selective retention of two dinoflagellates in a well-mixed estuarine embayment: the importance of vertical migration and surface avoidance. *Marine Ecology Progress Series* 25, 39–50.
- Anderson, D.M., Kulis, D.M., Binder, B.J., 1984. Sexuality and cyst formation in the dinoflagellate *Alexandrium tamarensis*: Cyst yield in batch cultures. *Journal of Phycology* 20 (3), 418–425.
- Anderson, D.M., Taylor, C.D., Armbrust, V.E., 1987. The effects of darkness and anaerobiosis on dinoflagellate cyst germination. *Limnology and Oceanography* 32 (2), 340–351.

- Anderson, D.M., Kulis, D.M., Doucette, G.J., Gallagher, J.C., Balech, E., 1994. Biogeography of toxic dinoflagellates in the genus *Alexandrium* from the northeastern United States and Canada. *Marine Biology* 120 (3), 467–478.
- Anderson, D.M., Keafer, B.A., Geyer, W.R., Signell, R.P., Loder, T.C., 2005a. Toxic *Alexandrium* blooms in the Gulf of Maine: the “plume advection hypothesis” revisited. *Limnology and Oceanography* 50 (1), 328–345.
- Anderson, D.M., Stock, C.A., Keafer, B.A., Bronzino, A.C., Matrai, P., Thompson, B., Keller, M., McGillicuddy, D.J., Hyatt, J., 2005b. *Alexandrium fundyense* cyst dynamics in the Gulf of Maine. *Deep-Sea Research Part II*, this issue [doi:10.1016/j.dsr2.2005.06.014].
- Bauerfeind, E., Elbrachter, M., Steiner, R., Thronsdon, J., 1986. Application of Laser Doppler Spectroscopy (LDS) in determining swimming velocities in motile phytoplankton. *Marine Biology* 93 (3), 323–327.
- Blumberg, A.F., Mellor, G.L., 1987. A description of a three-dimensional coastal ocean circulation model. In: Heaps, N. (Ed.), *Three-Dimensional Coastal Ocean Models*. American Geophysical Union, pp. 1–16.
- Blumberg, A.F., Signell, R.P., Jenter, H.L., 1993. Modelling transport processes in the coastal ocean. *Journal of Marine Environmental Engineering* 1, 31–52.
- Bretherton, F.P., Davis, R.E., Fandry, C.B., 1976. A technique for objective analysis and design of oceanographic experiments applied to MODE-73. *Deep-Sea Research II* 23 (7), 559–582.
- Brooks, D.A., 1985. Vernal circulation in the Gulf of Maine. *Journal of Geophysical Research* 90 (C3), 4687–4705.
- Brooks, D.A., 1994. A model study of the buoyancy-driven circulation in the Gulf of Maine. *Journal of Physical Oceanography* 24 (11), 2387–2412.
- Brooks, D.A., Townsend, D.W., 1989. Variability of the coastal current and nutrient pathways in the eastern Gulf of Maine. *Journal of Marine Research* 47 (2), 303–321.
- Cambell, R.G., Teegarden, G.J., Cembella, A.D., Durbin, E.G., 2005. Zooplankton grazing impacts on *Alexandrium* spp. in the near-shore environment of the Gulf of Maine. *Deep Sea Research II*, this issue [doi:10.1016/j.dsr2.2005.06.008].
- Carpenter, E.J., Guillard, R.R.L., 1971. Intraspecific differences in the nitrate half-saturation constants for three species of marine phytoplankton. *Ecology* 52 (1), 183–185.
- Churchill, J.H., Pettigrew, N.R., Signell, R.P., 2005. Structure and variability in the western Maine Coastal Current. *Deep Sea Research Part II*, this issue [doi:10.1016/j.dsr2.2005.06.019].
- Clark, H.L., Isern, A. (Eds.), 2003. Special issue: ocean observatories. *Oceanography* 16(4), 109pp.
- Conway, H.L., Harrison, P.J., 1977. Marine diatoms grown in chemostats under silicate or ammonium limitation. IV. Transient response of *Chaetoceros debilis*, *Skeletonema costatum*, and *Thalassiosira gravida* to a single addition of limiting nutrient. *Marine Biology* 43 (1), 33–43.
- Cook, R.D., Weisberg, S., 1982. Residuals and Influence in Regression. Chapman & Hall, New York.
- Cox, D.R., Hinkley, D.V., 1974. *Theoretical Statistics*. Chapman & Hall, London.
- Draper, N.R., Smith, H., 1981. *Applied Regression Analysis*. Wiley, New York.
- Droop, M.R., 1983. 25 years of algal growth kinetics, a personal view. *Botanica Marina* 26 (3), 99–112.
- Eppley, R.W., Thomas, W.H., 1969. Comparison of half-saturation “constants” for growth and nitrate uptake of marine phytoplankton. *Journal of Phycology* 5, 365–369.
- Eppley, R.W., Rogers, J.N., McCarthy, J.J., 1969. Half-saturation constants for uptake of nitrate and ammonium by marine phytoplankton. *Limnology and Oceanography* 14 (6), 912–920.
- Etheridge, S.M., Roesler, C.S., 2005. Effects of temperature, irradiance, and salinity on photosynthesis, growth rates, total toxicity, and toxin composition for *Alexandrium fundyense* isolates from the Gulf of Maine and Bay of Fundy. *Deep Sea Research II*, this issue [doi:10.1016/j.dsr2.2005.06.026].
- Ezer, T., Mellor, G.L., 1992. A numerical study of the variability and the separation of the Gulf Stream, induced by surface atmospheric forcing and lateral boundary flows. *Journal of Physical Oceanography* 22 (6), 660–682.
- Flynn, K., Jones, K.J., Flynn, K.J., 1996. Comparisons among species of *Alexandrium* (Dinophyceae) grown in nitrogen- or phosphorous-limiting batch culture. *Marine Biology* 126 (1), 9–18.
- Franks, P.J.S., Anderson, D.M., 1992a. Alongshore transport of a toxic phytoplankton bloom in a buoyancy current: *Alexandrium tamarensis* in the Gulf of Maine. *Marine Biology* 112 (1), 153–164.
- Franks, P.J.S., Anderson, D.M., 1992b. Toxic phytoplankton blooms in the Gulf of Maine: testing hypotheses of physical control using historical data. *Marine Biology* 112 (1), 165–174.
- Fung, I.Y., Harrison, D.E., Laci, A.A., 1984. On the variability of the net longwave radiation at the ocean surface. *Reviews of Geophysics and Space Physics* 22 (2), 177–193.
- Galperin, B., Kantha, L.H., Hassid, S., Rosati, A., 1988. A quasi-equilibrium turbulent energy model for geophysical flows. *Journal of Atmospheric Science* 45 (1), 55–62.
- Geraci, J.R., Anderson, D.M., Timperi, R.J., Staubin, D.J., Early, G.J., Prescott, J.H., Mayo, C.A., 1989. Humpback Whales (*Megaptera novaeangliae*) fatally poisoned by dinoflagellate toxin. *Canadian Journal of Fisheries and Aquatic Science* 46 (11), 1895–1898.
- Geyer, W.R., Signell, R.P., Fong, D.A., Wang, J., Anderson, D.M., Keafer, B.A., 2004. The freshwater transport and dynamics of the western Maine Coastal Current. *Continental Shelf Research* 24 (12), 1339–1357.
- He, R., Weisberg, R.H., 2002. West Florida shelf circulation and temperature budget for the 1999 spring transition. *Continental Shelf Research* 22 (5), 719–748.
- He, R., McGillicuddy, D.J., Lynch, D.R., Smith, K.W., Stock, C.A., Manning, J.P., in press. Data assimilative hindcast of the gulf of Maine coastal circulation. *Journal of Geophysical Research, Oceans*, 53pp.
- Hendry, R., He, I., 1996. Technical Report on Objective Analysis (OA) Project. Bedford Institute of Oceanography, Dartmouth, Nova Scotia, unpublished.
- Hetland, R.D., Signell, R.P., 2005. Modeling coastal current transport in the Gulf of Maine. *Deep-Sea Research II*, this issue [doi:10.1016/j.dsr2.2005.06.024].
- Houseman, E.A., Ryan, L.M., Coull, B.A., 2004. Cholesky residuals for assessing normal errors in a linear model with correlated outcomes. *Journal of the American Statistical Association* 99 (466), 383–394.
- Kamykowski, D., Reed, R.E., Kirkpatrick, G.J., 1992. Comparison of the sinking velocity, swimming velocity, rotation and

- path characteristics among six marine dinoflagellate species. *Marine Biology* 113 (2), 319–328.
- Keafer, B.A., Churchill, J.H., McGillicuddy, D.J., Anderson, D.M., 2005. Bloom development and transport of toxic *Alexandrium fundyense* populations within a nearshore coastal plume in the Gulf of Maine. *Deep Sea Research II*, this issue [doi:10.1016/j.dsr2.2005.06.016].
- Kuhl, M., Jorgensen, B.B., 1994. The light of microbenthic communities: Radiance distribution and microscale optics of sandy coastal sediments. *Limnology and Oceanography* 39 (6), 1368–1398.
- Langdon, C., 1987. On the causes of interspecific differences in the growth-irradiance relationships for phytoplankton. Part I. A comparative study of the growth irradiance relationships of three marine phytoplankton species: *Skelotonema costatum*, *Olithodiscus luteus* and *Gonyaulax tamarensis*. *Journal of Plankton Research* 9 (3), 459–482.
- Langdon, C., 1988. On the causes of interspecific differences in the growth-irradiance relationship for phytoplankton Part II. A general review. *Journal of Plankton Research* 10 (6), 1291–1312.
- Large, W.G., Pond, S., 1981. Open ocean momentum flux measurements in moderate to strong winds. *Journal of Physical Oceanography* 11 (3), 329–336.
- Large, W.G., Pond, S., 1982. Sensible and latent heat flux measurements over the ocean. *Journal of Physical Oceanography* 12 (5), 464–482.
- Lawson, L.M., Spitz, Y.H., Hofmann, E.E., Long, R.B., 1995. A data assimilation technique applied to a predator–prey model. *Bulletin of Mathematical Biology* 57 (4), 593–617.
- Lawson, L.M., Hofmann, E.E., Spitz, Y.H., 1996. Time series sampling and data assimilation in a simple marine ecosystem model. *Deep Sea Research II* 43 (2–3), 625–651.
- Liebig, J., 1845. *Chemistry and its Applications to Agriculture and Physiology: On Chemical Processes in the Nutrition of Vegetables*. L. Playfair, Peterson, PA.
- Lomas, M.W., Glibert, P.M., 2000. Comparison of nitrate uptake, storage, and reduction in marine diatoms and flagellates. *Journal of Phycology* 36 (5), 903–913.
- Luerssen, R.M., Thomas, A.C., Hurst, J.W., 2005. Relationships between satellite-measured thermal features and *Alexandrium*-imposed toxicity in the Gulf of Maine. *Deep Sea Research II*, this issue [doi:10.1016/j.dsr2.2005.06.025].
- Lynch, D.R., Naimie, C.E., 1993. The M2 tide and its residual on the outer banks of the Gulf of Maine. *Journal of Physical Oceanography* 23 (10), 2222–2253.
- Lynch, D.R., Naimie, C.E., 2002. Hindcasting the Georges Bank circulation, Part II: wind-band inversion. *Continental Shelf Research* 22 (15), 2191–2224.
- Lynch, D.R., Holboke, M.J., Naimie, C.E., 1997. The Maine coastal current: spring climatological circulation. *Continental Shelf Research* 17 (6), 605–634.
- MacIntyre, J.G., Cullen, J.J., Cembella, A.D., 1997. Vertical migration, nutrition and toxicity in the dinoflagellate *Alexandrium tamarensis*. *Marine Ecology Progress Series* 148 (1–3), 201–216.
- MacIsaac, J.J., Grunseich, G.S., Glover, H.J., Yentsch, C.M., 1979. Light and nutrient limitation in *Gonyaulax excavata*: nitrogen and carbon trace results. In: Taylor, D.L., Seliger, H.H. (Eds.), *Toxic Dinoflagellate Blooms: Proceedings of the Second Conference on Toxic Dinoflagellate Blooms*. Elsevier/North-Holland, Key Biscayne, Florida, pp. 107–110.
- Marshall, H.G., 1984. Phytoplankton distribution along the eastern coast of the USA. Part V. Seasonal density and cell volume patterns for the northeastern continental shelf. *Journal of Plankton Research* 6 (1), 169–193.
- Martorano, C.D., Loder, T.C., 1997. Nutrient dynamics during blooms of *Alexandrium* spp. in the southwestern Gulf of Maine. Masters Thesis, University of New Hampshire, Biogeochemical Systems Center, Durham, NH, USA, unpublished.
- Matrai, P., Thompson, B., Keller, M.D., 2005. *Alexandrium* spp. from eastern Gulf of Maine: circannual excystment of resting cysts. *Deep Sea Research II*, this issue [doi:10.1016/j.dsr2.2005.06.013].
- McGillicuddy, D.J., Lynch, D.R., Moore, A.M., Gentleman, W.C., Davis, C.S., Meise, C.J., 1998. An adjoint data assimilation approach to the diagnosis of physical and biological controls of *Pseudocalanus* spp. in the Gulf of Maine-Georges Bank region. *Fisheries Oceanography* 7 (3–4), 205–218.
- McGillicuddy, D.J., Signell, R.P., Stock, C.A., Keafer, B.A., Keller, M.D., Hetland, R.D., Anderson, D.M., 2003. A mechanism for offshore initiation of harmful algal blooms in the coastal Gulf of Maine. *Journal of Plankton Research* 25 (8), 1131–1139.
- McGillicuddy, D.J., Anderson, D.M., Lynch, D.R., Townsend, D.W., 2005. Mechanisms regulating the large-scale seasonal fluctuations of *Alexandrium fundyense* blooms in the Gulf of Maine: results from a physical–biological model. *Deep Sea Research II*, this issue [doi:10.1016/j.dsr2.2005.06.021].
- Mellor, G.L., Yamada, T., 1982. Development of a turbulence closure model for geophysical fluid problems. *Reviews of Geophysical and Space Physics* 20, 851–875.
- Naimie, C.E., Loder, J.W., Lynch, D.R., 1994. Seasonal variation in the three-dimensional residual circulation on Georges Bank. *Journal of Geophysical Research* 99 (C8), 15,967–15,989.
- Pettigrew, N., Townsend, D., Xue, H., Wallinga, J., Brickley, P., Hetland, R., 1998. Observations of the eastern Maine Coastal Current and its offshore extensions in 1994. *Journal of Geophysical Research* 103 (C13), 30,623–30,639.
- Pettigrew, N.R., Churchill, J.H., Janzen, C.D., Mangum, L.J., Signell, R.P., Thomas, A.C., Townsend, D.W., Wallinga, J.P., Xue, H., 2005. The kinematic and hydrographic structure of the Gulf of Maine Coastal Current. *Deep Sea Research II*, this issue [doi:10.1016/j.dsr2.2005.06.033].
- Platt, T., Jassby, A.D., 1976. The relationship between photosynthesis and light for natural assemblages of coastal marine phytoplankton. *Journal of Phycology* 12 (4), 421–430.
- PO.DAAC, 1985. AVHRR Oceans Pathfinder global equal-angle best SST NOAA, NASA. <http://www.podaac.jpl.nasa.gov>.
- Poulton, N.J., 2001. Physiological and behavioral diagnostics for nitrogen limitation for the toxic dinoflagellate *Alexandrium fundyense*. Ph.D. Thesis, Woods Hole/MIT Joint Program, Biological Oceanography, Woods Hole, MA, unpublished.
- Poulton, N.J., Keafer, B.A., Anderson, D.M., 2005. Toxin variability in natural populations of *Alexandrium fundyense* in Casco Bay, Maine—evidence of nitrogen limitation. *Deep Sea Research II*, this issue [doi:10.1016/j.dsr2.2005.06.029].
- Prakash, A., 1967. Growth and toxicity of a marine dinoflagellate, *Gonyaulax tamarensis*. *Journal of the Fisheries Research Board of Canada* 24 (7), 1589–1606.

- Press, W.H., Flannery, B.P., Teukolsky, S.A., Vetterling, W.T., 1985. Numerical Recipes. The Art of Scientific Computing. Cambridge University Press, Cambridge.
- Scholin, C.A., Hallegraeff, G.M., Anderson, D.M., 1995. Molecular evolution of the *Alexandrium tamarense* “species complex” (Dinophyceae): Dispersal in the North American and West Pacific regions. *Phycologia* 34 (6), 472–485.
- Shull, D.H., 2001. Transition-matrix model of bioturbation and radionuclide diagenesis. *Limnology and Oceanography* 46 (4), 905–916.
- Shumway, S.E., Sherman-Caswell, S., Hurst, J.W., 1988. Paralytic shellfish poisoning in Maine: Monitoring a monster. *Journal of Shellfish Research* 7 (4), 643–652.
- Signell, R.P., Jenter, H.L., Blumberg, A.F., 1993. Modeling the seasonal circulation in Massachusetts Bay. In: *Estuarine and Coastal Modeling III*. Oak Brook, Illinois, pp. 578–590.
- Smagorinsky, J., 1963. General circulation experiments with the primitive equations, I. The basic experiment. *Monthly Weather Review* 91, 99–164.
- Sommer, U., 1991. A comparison of the Droop and Monod models of nutrient limited growth applied to natural populations of phytoplankton. *Functional Ecology* 5 (4), 535–544.
- Teegarden, G.J., Cambell, R.G., Durbin, E.G., 2001. Zooplankton feeding behavior and particle selection in natural phytoplankton assemblages containing toxic *Alexandrium* spp. *Marine Ecology Progress Series* 218, 213–226.
- Teegarden, G.J., Cembella, A.D., 1996. Grazing of toxic dinoflagellates, *Alexandrium* spp., by adult copepods of coastal Maine: implications for the fate of paralytic shellfish toxins in marine food webs. *Journal of Experimental Marine Biology and Ecology* 196 (1–2), 145–176.
- Townsend, D.W., Pettigrew, N.R., Thomas, A.C., 2001. Offshore blooms of the red tide dinoflagellate *Alexandrium* sp., in the Gulf of Maine. *Continental Shelf Research* 21 (4), 347–369.
- Turner, J.T., Borkman, D.G., 2005. Impact of zooplankton grazing on *Alexandrium* spp. blooms in the offshore Gulf of Maine. *Deep Sea Research II*, this issue [doi:10.1016/j.dsr2.2005.06.011].
- Turner, J.T., Tester, P.A., 1997. Toxic marine phytoplankton, zooplankton grazers, and pelagic food webs. *Limnology and Oceanography* 5 (2), 1203–1214.
- Watrass, C.J., Chisholm, S.W., Anderson, D.M., 1982. Regulation of growth in an estuarine clone of *Gonyaulax tamarensis* Lebour: salinity-dependent temperature responses. *Journal of Experimental Marine Biology and Ecology* 62 (1), 25–37.
- Wheatcroft, R.A., Martin, W.H., 1996. Spatial variation in short-term (^{234}Th) sediment bioturbation intensity along an organic carbon gradient. *Journal of Marine Research* 54 (4), 763–792.
- White, A.W., Fukuhara, O., Anraku, M., 1989. Mortality of fish larvae from eating toxic dinoflagellates or zooplankton containing dinoflagellate toxins. In: Okaichi, T., Anderson, D.M., Nemoto, T. (Eds.), *Red Tides: Biology, Environmental Science, and Toxicology*. Elsevier, New York, pp. 395–398.
- Wunsch, C., 1996. *The Ocean Circulation Inverse Problem*. Cambridge University Press, New York.